MEASUREMENT SCIENCE REVIEW, **17**, (2017), No. 6, 250-256

DE GRUYTER OPEN

MEASUREMENT SCIENCE REVIEW

Journal homepage: http://www.degruyter.com/view/j/msr

ISSN 1335-8871

Spectral Analysis of Pressure, Noise and Vibration Velocity Measurement in Cavitation

Jana Jablonská[1], Miroslav Mahdal[2], Milada Kozubková[1]

[1] *Department of Hydromechanics and Hydraulic Equipment, Faculty of Mechanical Engineering, VŠB - Technical University of Ostrava, 17. listopadu 15, 708 33 Ostrava - Poruba, Czech Republic, jana.jablonska@vsb.cz*
[2] *Department of Control Systems and Instrumentation, Faculty of Mechanical Engineering, VŠB, - Technical University of Ostrava, 17. listopadu 15, 708 33 Ostrava - Poruba, Czech Republic*

The article deals with experimental investigation of water cavitation in the convergent-divergent nozzle of rectangular cross-section. In practice, a quick and simple determination of cavitation is essential, especially if it is basic cavitation or cavitation generated additionally by the air being sucked. Air influences the formation, development and size of the cavity area in hydraulic elements. Removal or reduction of the cavity area is possible by structural changes of the element. In case of the cavitation with the suction air, it is necessary to find the source of the air and seal it. The pressure gradient, the flow, the oxygen content in the tank, and hence the air dissolved in the water, the air flow rate, the noise intensity and the vibration velocity on the nozzle wall were measured on laboratory equipment. From the selected measurements the frequency spectrum of the variation of the water flow of the cavity with cavitation without air saturation and with air saturation was compared and evaluated.

Keywords: Cavitation, noise, vibration, spectral analysis, CFD.

1. INTRODUCTION

Cavitation noise and vibrations result from the formation, growth and collapse of the cavitation bubbles. In particular, bubble collapse is accompanied by high flow velocities and high fluid pressure in the area of the cavitation bubbles, as a result of which compressive forces are induced [6], [9]. There are a large number of these bubbles in the cavitation area that interact with each other. According to literature [2], small cavitation bubbles have a frequency of their occurrence and extinction of up to 3 MHz, whereas large pulsating bubble structures (in the developed cavitation) can have a frequency of tens of Hz. This is used to identify cavitation in hydraulic elements. Appropriate location of sensors on the machine can determine the position of the cavity [3]. It is reported in the literature [1] that the origin of cavitation is characterized by frequencies ranging from 1 kHz to 20 kHz, developed cavitation ranging from 20 Hz to 500 Hz. In the literature [4], cavitation was detected at the frequency of 40 kHz and it was proved that at lower frequencies the peak of the frequency spectrum of cavitation noise is of very little significance. Frequency values depend on the specific equipment and operating conditions.

The intensity of cavitation noise increases from the initial cavitation to fully developed cavitation and then decreases rapidly. Thus, the maximum noise intensity appears before fully developed cavitation. In addition, the maximum cavitation wear consistency with maximum cavitation noise [1] is evident. The increase of cavitation vibration, depending on the level of cavitation, is similar to that of cavitation noise, i.e. near the fully developed cavitation vibration is the maximum.

For the evaluation of noise, the sound pressure level in [dB] [5] is introduced, which is given by the relation

$$L_p = 20 \log\left(\frac{p}{p_0}\right) \tag{1}$$

where p is the sound pressure, $p_0 = 2 \cdot 10^{-5}$ Pa is the reference value of sound pressure. It is possible to use the acoustic intensity I [W/m^2], which is a vector defining the flow of acoustic energy per unit area in a direction perpendicular to this area. From this definition, its relation to the acoustic power W [W] is

$$W = \int_S I \cdot \mathrm{d}S \tag{2}$$

Parallel to cavitation noise, cavitation phenomena cause device vibration. According to the literature [1], significant vibration frequencies range from 25 Hz to 1000 Hz, while the other frequencies associated with cavitation bubble formation and disappearance are noticeable but with less amplitude.

DOI: 10.1515/msr-2017-0030

2. EXPERIMENTAL AND MATHEMATICAL METHODS

Physical experiment

Cavitation measurements were performed with the water flow in the convergent-divergent nozzle of rectangular cross section (CDN), its basic dimensions are shown in Fig.1.

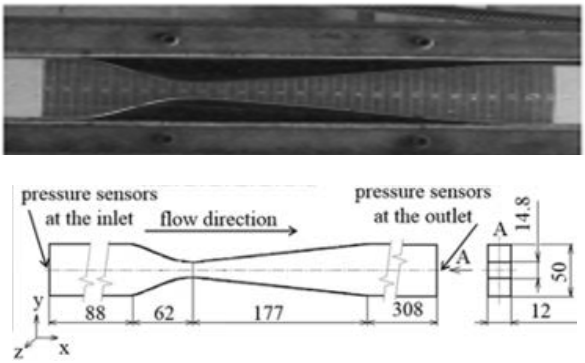

Fig.1. Photo and schema of convergent-divergent nozzle of rectangular cross section.

Cavitation was observed visually, by noise and vibration. The water flow was changed using a frequency converter from 12 Hz to 36 Hz. The measurement range was limited by the structure and parameters of the equipment material. A number of measurements were also carried out on the flow of water with added air.

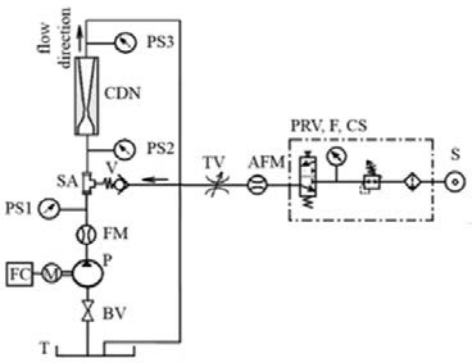

Fig.2. Measuring circuit T – tank, BV - ball valve, P- water pump, M - electric motor, FC - frequency converter, FM - inductive flowmeter, PS - pressure sensors, CDN - measured object – convergent-divergent nozzle of rectangular cross-section, SA air saturation, V – one-way valve, TV – throttle valve to control air flow rate, AFM – air flowmeter, PRV, F, CS – pressure regulating valve with a filter unit and a condensate separator, S – compressed air source with a pressure gauge.

The scheme of measuring hydraulic circuit is evident from the diagram in Fig.2. The liquid (density $\rho = 1001$ kg.m^{-3}, viscosity $\nu = 1.10^{-6}$ m^{2}s^{-1}) is pumped into the circuit by a pump (P) which is connected to the tank (T) with water. A ball valve (BV) is located between the tank and the pump. The pump is driven by an electric motor (M) with speed control via a frequency converter (FC). An inductive flowmeter (FM) and a pressure gauge (PS1) are connected behind the pump. Attached air saturation device (SA) consists of air flow control valve (TV), air flowmeter (AFM), pressure control valve (PRV) with filter unit (F), condensate separator (CS), and compressed air source (S). The basic element of the circuit is the transparent convergent-divergent nozzle of the rectangular cross-section (CDN) to generate cavitation. Pressure sensors are placed before (PS2) and behind (PS3) the CDN nozzle. A 4507 B 004 accelerometer from Brüel & Kjær is attached to the nozzle wall. The MiniSPL Noise Sensor is placed approximately 0.4 m in front of the nozzle. The Oxymax W COS61 water sensor was placed in the tank, which also sensed the temperature of the liquid. The result of the measurement was a signal directly proportional to the concentration of oxygen in the medium and the temperature of the medium. [7] The temperature of the medium did not change very much during the measurement, it was 25°C.

Table 1. Measured values for variant I - without added air, II - with added air.

		Variant I - without added air			
f [Hz]	p_2 [kPa]	p_3 [kPa]	Δp [kPa]	$Q_{m,w}$ [kg/s]	C_{O2} [mg/l]
12	116	103	13	1.153	7.02
14	122	107	15	1.380	7.03
16	128	111	17	1.678	7.04
18	136	115	21	1.920	7.04
20	144	121	23	2.219	7.03
22	154	126	28	2.408	7.03
24	165	131	34	2.696	7.04
26	184	137	47	2.838	7.05
28	204	142	62	2.974	7.04
30	225	147	78	3.269	7.02
32	248	151	97	3.421	7
34	273	160	113	3.673	6.94
36	298	169	129	3.925	6.9

		Variant II - with added air				
f [Hz]	p_2 [kPa]	p_3 [kPa]	Δp [kPa]	$Q_{m,w}$ [kg/s]	C_{O2} [mg/l]	$Q_{m,air,N}$ [kg/s]
12	115	102	13	1.573	6.59	$1.67 \cdot 10^{-5}$
14	120	104	16	1.842	6.65	$1.63 \cdot 10^{-5}$
16	127	108	19	2.120	6.71	$1.45 \cdot 10^{-5}$
18	134	113	21	2.395	6.75	$1.25 \cdot 10^{-5}$
20	142	117	25	2.645	6.86	$1.51 \cdot 10^{-5}$
22	155	123	32	2.834	6.95	$1.37 \cdot 10^{-5}$
24	172	126	46	3.029	7.01	$1.33 \cdot 10^{-5}$
26	191	131	60	3.200	7.09	$1.29 \cdot 10^{-5}$
28	211	136	75	3.371	7.15	$1.21 \cdot 10^{-5}$
30	233	135	98	3.553	7.18	$1.49 \cdot 10^{-5}$
32	256	140	116	3.752	7.23	$1.31 \cdot 10^{-5}$
34	280	147	133	3.938	7.23	$1.47 \cdot 10^{-5}$
36	305	148	157	4.138	7.2	$1.05 \cdot 10^{-5}$

For each engine speed (i.e. flow rate) set, all relative pressures, noise intensity (MiniSPL Noise Sensor) and vibration velocities (4507 B 004 accelerometer) were recorded during the measurement on the computer with a given sampling frequency and subsequently evaluated. The tables show average pressure values measured by commonly available gauges with a time step 0.001 s.

In Table 1. the measured average values of hydraulic variables (p_2 – pressure before CDN, p_3 – pressure behind CDN, $\Delta p = p_2 - p_3$ - pressure drop, $Q_{m,w}$ – water mass flow rate, C_{O2} – concentration of oxygen in the tank, $Q_{m,air,N}$ – added air mass flow rate under normal conditions) for variant without added air and variant with added air were evaluated.

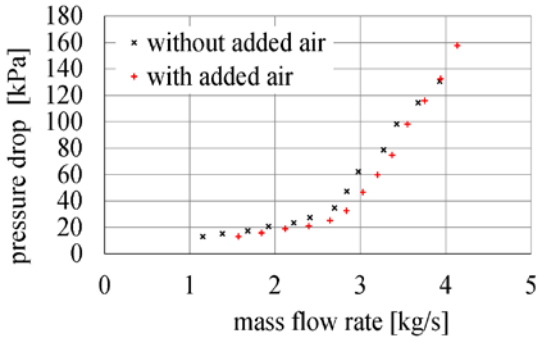

Fig.3. Dependence of pressure drop on mass flow rate for two variants of measurement.

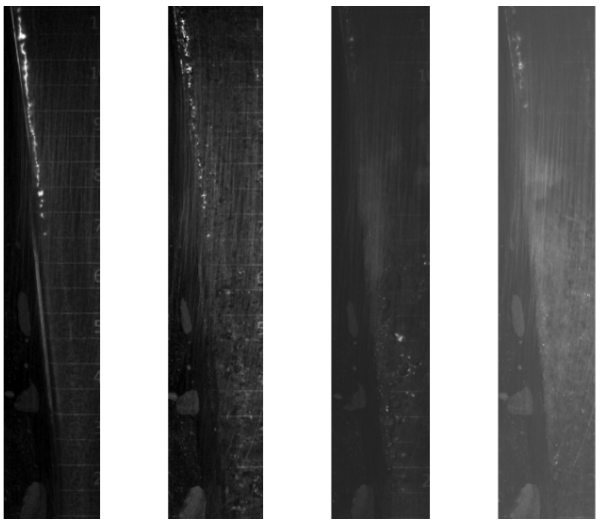

Fig.4. Flowing without and with added air, without and with cavitation.

Fig.3. shows the dependence of the pressure drop on the CDN nozzle vs. the mass flow rate for both measured variants. A slower increase of the pressure drop in the lower flow area is in the non-cavitation flow. Then there is a sharp increase in the pressure gradient, which corresponds to the flow with cavitation (the flow is greater than 2.4 kg/s). Additionally, at a flow rate of up to 3.9 kg/s with cavitation and no added air, the pressure drop on CDN is higher than that in variant II with added air. At higher flow rates and developed cavitation (flow rate is greater than 3.9 kg/s) it is the opposite, i.e. the pressure drop is higher in the case of flow with the added air than in the case of flow without added air. This phenomenon was also reported during further measurements.

The images of the CDN nozzle are illustrated in Fig.4., image a) presents a flow condition without cavitation and without added air, b) without cavitation and with added air, c) with cavitation and without added air, and d) with cavitation and with added air.

Initial cavitation was observed by sight and determined by noise. The basic assessment is usually performed using dimensionless parameters, i.e. dependence of Reynolds number $\mathrm{Re} = \frac{v_{max} d}{\nu}$ versus cavitation number $\sigma = \frac{2(p_{out} - p_n)}{\rho v_{max}^2}$, see Fig.5. [8].

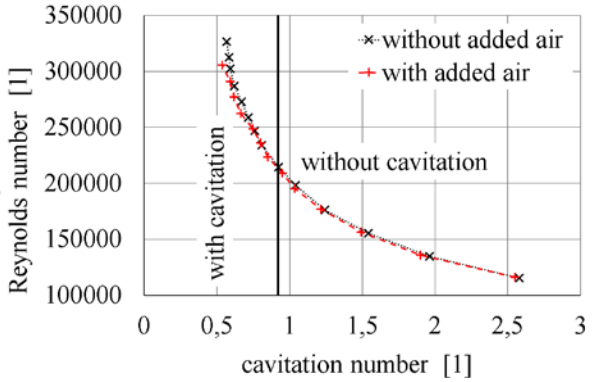

Fig.5. Reynolds number versus cavitation number (p_{out} – mean static pressure at the outlet from the nozzle, p_n – saturated pressure at given conditions, ρ - density of water, ν - kinematic viscosity of water, d – hydraulic diameter of the narrow cross section, v_{max} – velocity in narrow cross section).

In the case of variant I without added air, the initial cavitation was detected at higher engine revolutions (speeds) than 22 Hz, i.e. with a cavitation number lower than 0.92. The value of the cavitation number decreases with the added air. For the same Reynolds number, the cavitation number is higher for the variant with no added air. With the same cavitation number, the Reynolds number in the cavitation area is higher for the variant without added air. In an area without cavitation, the previous claim is unambiguous.

Fig.6. shows the air volume fraction at pressure near the bottom of the tank (i.e. 111.6 kPa) depending on the cavitation number. For variant I, the volume fraction of the dissolved air measured in the tank is plotted. For variant II, the sum of the volume fraction of the dissolved air in the tank and the volume fraction of the added air is shown. The volume fraction of the dissolved air in the tank was almost the same for both variants. The volume fraction of the added air into the system increases with the increasing cavitation number.

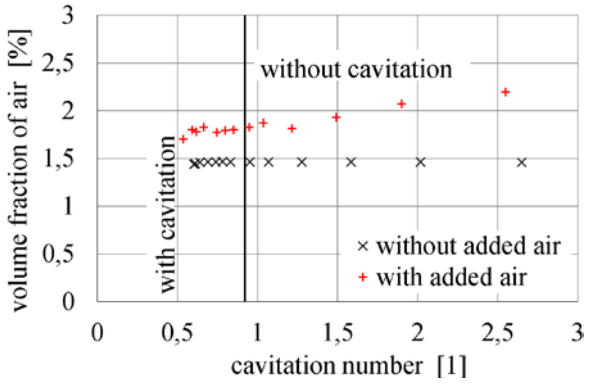

Fig.6. Volume fraction of air versus cavitation number.

Fig.7. shows the dependence of the loss coefficient on the cavitation number for both variants (variant I - without added air, variant II - with added air). Loss coefficient is defined by formula $\zeta = \frac{2p_2}{\rho v_{in}^2}$, $v_{in} = \frac{4Q_{m,w}}{\rho \pi d^2}$.

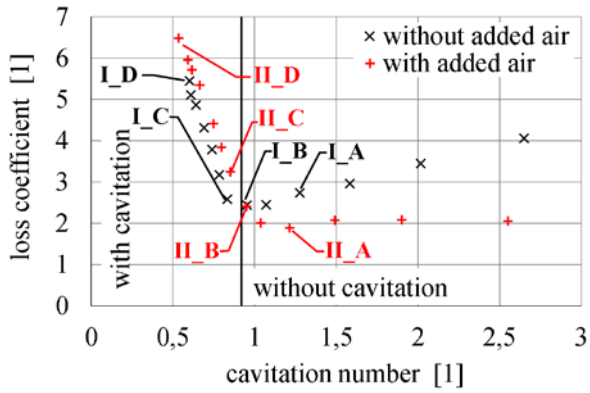

Fig.7. Loss coefficient versus cavitation number (marked variants will be solved later).

The loss coefficient in the cavitation-free flow area decreases with the decreasing cavitation number. In the cavitation flow area, the loss coefficient increases with the decreasing cavitation number. The lowest loss coefficient occurs in a critical cavitation number.

Marked variants in Fig.7. are further evaluated. Variant A represents flow without cavitation, B - flow at the cavitation interface, C - flow with initial cavitation, D - flow with fully developed cavitation.

Mathematical modeling

A 3D simulation of flow for variant I (considering air released from the fluid and no added air) was conducted with a multiphase turbulent RNG k-ε model [10], [11], [12], [15]. The boundary condition at the input was defined by the mass flow rate of water, vapor and possibly air, at the output as pressure outlet. Mass flow rates and pressure values for boundary conditions were determined as average values from measurements.

3. RESULTS

Evaluation of the frequency spectrum of the measured pressure

In Fig.8. and Fig.9. the frequency spectra from the measured pressures at the inlet to the CDN nozzle (i.e., pressure p_2, see Table 1.) are evaluated. The frequency range is limited by the sampling frequency of the pressure. The pressure was scanned within 0.001 seconds, so the frequency is limited to 400 Hz.

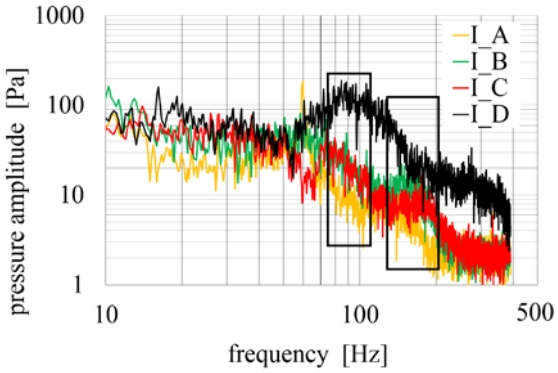

Fig.8. Pressure amplitude vs. frequency at inlet of the CDN nozzle, variant I – without the added air.

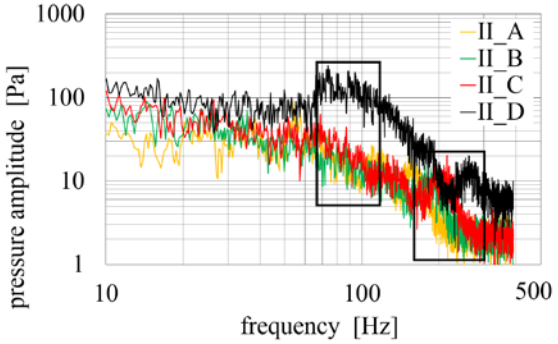

Fig.9. Pressure amplitude vs. frequency at inlet of the CDN nozzle, variant II – with the added air.

In variant I - for D there is a significant frequency around 87 Hz, for A, B, C this frequency is not so pronounced. Significant frequencies for B, C, and D range from 151 Hz to 172 Hz. The obtained frequencies specify the vortex structures due to the flow around the CDN nozzle and possibly cavitation.

In variant II - for all four measurements (with added air) there is a significant frequency in the range from 65 Hz to 75 Hz. Other significant frequencies are in the range from 117 Hz to 158 Hz, where it is noticeable that with increasing flow rate, this more significant frequency moves to the right. In addition, the frequencies are affected by the added air against variation I.

In the fully developed cavitation of variants I_D and II_D, more pronounced frequencies of the vortex cavitation structures are evident.

Evaluation of frequency spectrum of noise intensity and vibration velocity

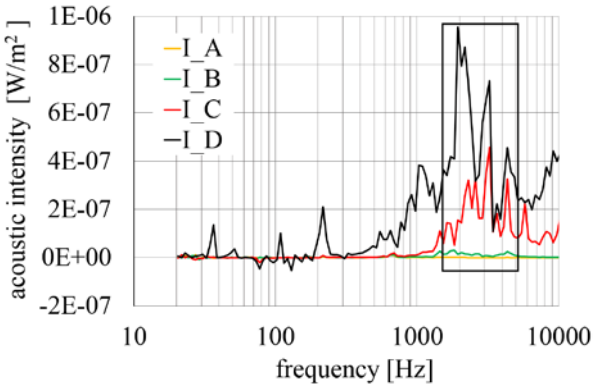

Fig.10. Acoustic intensity vs. frequency, variant I – without the added air.

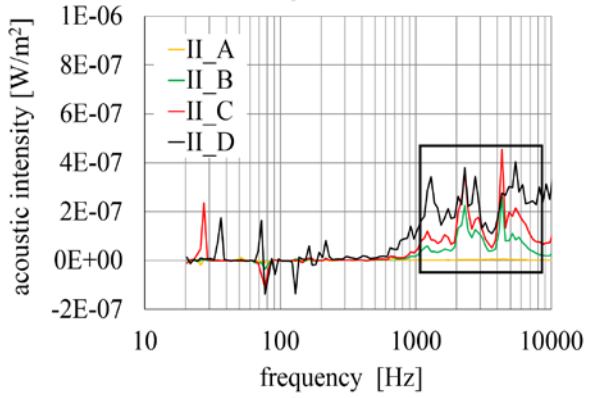

Fig.11. Acoustic intensity vs. frequency, variant II – with the added air.

Fig.10. and Fig.11. show the frequency spectra obtained from noise measurements. When measuring noise intensity, frequencies of less than 300 Hz are not considered, as they are influenced by the laboratory environment. The frequencies determining the formation and destruction of cavitation bubbles are significant. For variants I_A, I_B, and II_A (flow without cavitation), the amplitude of the noise intensity is very small. However, for variants I_C, II_B, and II_C, significant frequencies are 2300 Hz (vapor cavitation) and 4340 Hz (air cavitation). In variant I_D, the amplitudes of the noise intensity are more pronounced, since it is a fully developed cavitation, significant frequencies are in the range from 1900 Hz to 4300 Hz. Variants II_D have significant frequencies in the range of 1300 Hz to 5500 Hz. In case of variants II with added air there are significantly lower amplitudes of the noise intensity in the cavitation area, as the added air suppresses the noise intensity. Therefore, in terms of cavitation identification, noise measurement is not the most appropriate.

Variable frequency spectra of vibration velocity (Fig.12, Fig.13.) show low frequencies (up 500 Hz) consistent with the pressure spectral analysis (see Fig.8., Fig.9.) and high frequencies that can be obtained from the records of the noise intensity (see Fig.10., Fig.11.).

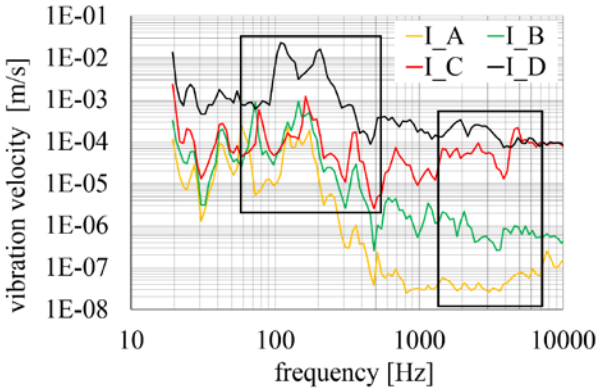

Fig.12. Vibration velocity vs. frequency, variant I – without the added air.

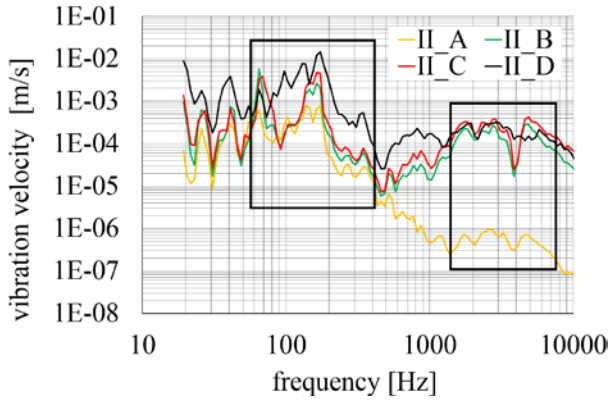

Fig.13. Vibration velocity vs. frequency, variant II – with the added air.

Approximately from 500 Hz, the frequency spectrum of measurements I_A, I_B, and II_A is still decreasing (the turbulence effect) compared to other measurements, and the amplitude of the vibration velocity is very low. It is clear from this trend that cavitation does not occur in these measurements. The added air promotes cavitation even at lower flow rates and, consequently, higher frequencies (over 1000 Hz) are better seen.

- Variant I - in the spectrum A, B, and C the significant frequencies ranging from 70 Hz to 90 Hz, the frequencies ranging from 163 Hz to 172 Hz and around 365 Hz are evident. For spectrum D, there are three main frequencies 115 Hz, 217 Hz, and 365 Hz. The cavitation bubble generation and extinction frequencies are in the range from 2000 Hz to 5000 Hz, while the spectrum amplitudes gradually increase with increasing flow rate.
- Variant II - all spectra have a significant peak in the range of 65 Hz – 70 Hz, which characterize the vortex structures at the flow around the nozzle and all spectra have a significant peak in the range from 160 Hz to 170 Hz and also around 365 Hz. Significant frequencies for B, C, and D are around 1940 Hz and 2900 Hz, indicating the predominant vapor cavitation. For spectra B and C there is also a significant frequency around 5300 Hz, but for D this frequency is shifted to 6100 Hz. These frequencies indicate

increased air cavitation. The amplitude of the spectra B, C, and D above 1000 Hz is approximately the same due to cavitation and the influence of added air.

Higher frequencies are approximately the same as those obtained from noise intensity measurements, but the amplitudes are not so pronounced.

Mathematical *modeling*

In Fig.14. the tested mathematical models are evaluated and compared with the measurement.

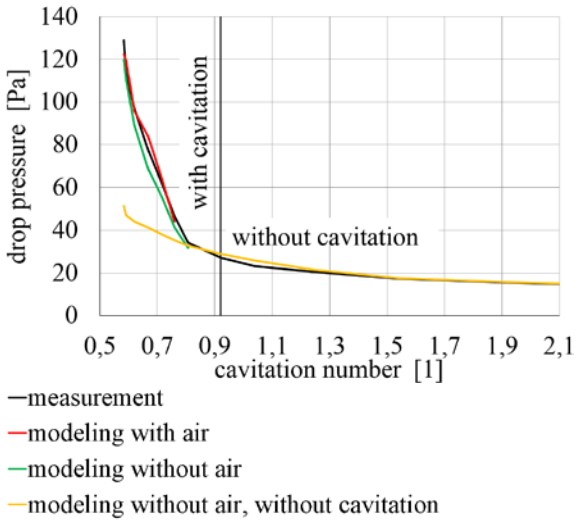

Fig.14. Pressure drop versus cavitation number for measurement and modeling variant.

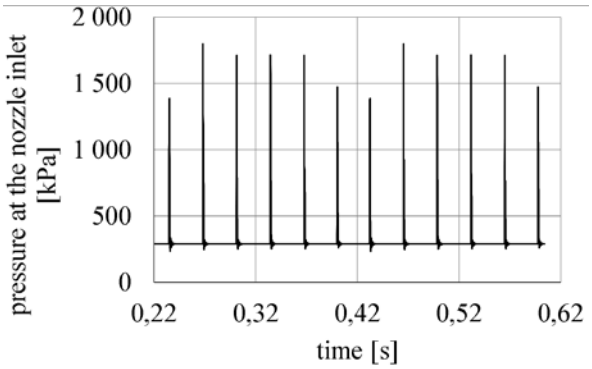

Fig.15. Record of pressure on CDN nozzle input obtained from mathematical modeling for variant I_D.

At first, the tasks (Fig.14., yellow line) were solved by the simplest stationary, two-phase (water, vapor), non-cavitation model. The deviation between the pressure drop and the measurement for the non-cavitation area ranged from 0 to 5 %, in the cavitation area the pressure drop deviation was up to 65 %. Therefore, it was necessary to use the cavitation Schnerr Sauer non-stationary model with a time step of 10^{-5} s in the area of cavitation flow due to the evaluation of the results by spectral analysis [14], [16], see Fig.14., green line. The deviation was up to 15 %. For further refinement, the model was extended to a cavitation three-phase model (water, vapor, air). In the inlet boundary condition, the mass air flow rate was defined as 0.1 % of volume fraction. The deviation between the calculation and the measurement was within 5 % (see Fig.14., red line). The value of the undissolved air released from the liquid in the tank has been estimated. The modeling methodology for the added air variant will be the same and will be tested in the future.

Fig.15. shows the record of pressure at the CDN nozzle input obtained from the modeling for variant I_D.

Subsequently, the frequency spectrum was evaluated from this record, see Fig.16. Significant frequencies in the box are identical to the significant frequencies gained from noise and vibration measurement.

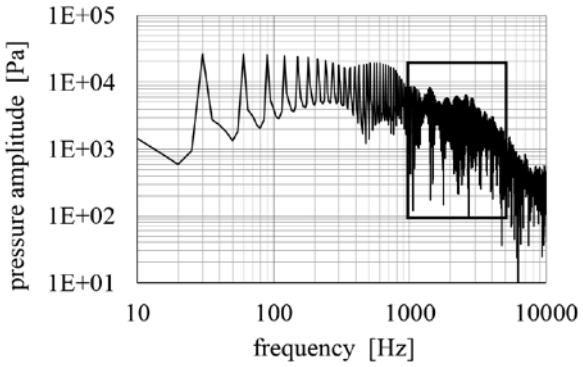

Fig.16. Pressure amplitude for variant I_D vs. frequency at CDN nozzle inlet (spectral analysis).

4. Discussion / conclusions

The article deals with the possibilities of detection of cavitation in hydraulic elements by means of spectral analysis determined by pressure, noise, and vibration measurement. The described methods are simple, cheap and fast. However, individual methods give results over a limited range of frequencies due to the characteristics of the gauges used.

Fig.17. shows all the frequency spectra (from measured inlet pressure, modeled input pressure, vibration velocity, and noise intensity) for variant I_D. The arrows show the previously described significant frequencies from the individual measurements. It can be clearly stated that to obtain information on the frequencies of the vortex structures with the developed cavitation in the case of flow through the nozzle, it is sufficient to measure the pressure by means of commonly used gauges. If it is necessary to obtain higher frequencies related to cavitation bubble formation and extinction, it is advisable to use noise intensity measurement. Measurement of vibration velocity gives sufficient information over the entire frequency range, but not so pronounced in amplitude. Mathematical modeling records the high frequencies associated with cavitation bubble formation and cessation, but a suitable model [10], [13], [14], the network, and the time step need to be chosen appropriately. Another disadvantage of mathematical modeling is the time consuming calculation. However, with newly developed elements, mathematical modeling is necessary.

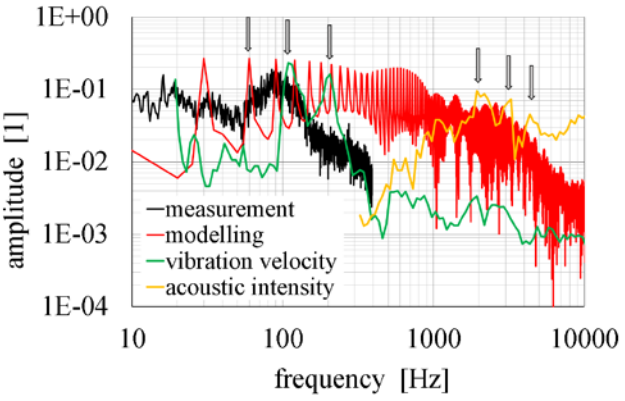

Fig.17. Spectral analysis of variant I_D.

The frequency spectrum obtained from the measured pressure compared to vibration velocity (liquid-plexiglass) and noise intensity (liquid-plexiglass-air transfer) shows a slight variation due to measurements in different environments.

Due to the measurement, an earlier indication of the initial cavitation in variant II_B was noted, indicating that the added air supports the formation and development of air cavitation and suppresses vapor cavitation. However, air cavitation does not have such a destructive effect on material as vapor cavitation. Vapor cavitation is more dangerous for hydraulic components.

When comparing the noise intensity for fully developed cavitation (variant D), it is clear that the added air suppresses the noise intensity amplitude and simultaneously suppresses vapor cavitation. This claim, however, is not apparent from the observation of the cavitation cloud with the naked eye.

From the thesis it follows that it will be necessary to deal with further mathematical methods for the theoretical mastering of cavitation.

ACKNOWLEDGEMENT

The work presented in this paper was supported by a grant SGS „Research on dynamics of fluid systems“. SP2017/103.

This work was supported by The Ministry of Education, Youth and Sports from the Large Infrastructures for Research, Experimental Development and Innovations project “Innovations National Supercomputing Centre – LM2015070”.

REFERENCES

[1] Noskievič, J. (1990). *Cavitation in Hydraulic Machinery and Equipment.* Prague, Czech Republic: SNTL. (in Czech).

[2] Pearsall, I. S. (1966). Acoustic detection of cavitation. *Proceedings of the Institution of Mechanical Engineers, Conference Proceedings*, 181 (1).

[3] Brdička, M., Samek, L., Taraba, O. (1981). *Cavitation: Diagnostics and Technical Use).* Prague, Czech Republic: SNTL. (in Czech).

[4] Deeprose, W.M., King, N.W., McNulty, P.J. Pearsall, I.S. (1974). Cavitation noise, flow noise and erosion. In *Proceedings of the Conference on Cavitation.* London, UK: Institute of Mechanical Engineers, 373-381.

[5] Smetana, C. (1998). *Noise and Vibration: Measurement and Evaluation*. Prague, Czech Republic: Sdělovací technika. (in Czech)

[6] Brennen, Ch.E. (1995). *Cavitation and Bubble Dynamics.* Oxford University Press.

[7] Jablonská, J., Kozubková, M., Himr, D., Weisz, M. (2016). Methods of experimental investigation of cavitation in a convergent-divergent nozzle of rectangular cross section. *Measurement Science Review*, 16 (4), 197-204.

[8] Čarnogurská, M., Příhoda, M., Popčáková, D. (2010). Modelling the flow conditions in the tunnel and its reduced model. *Journal of Mechanical Science and Technology*, 24 (12), 2479-2486.

[9] Meng, J., Liu, Z., An, K., Yuan, M. (2017). Simulation and optimization of throttle flowmeter with inner-outer tube element. *Measurement Science Review*, 17 (2), 68-75.

[10] Knížat, B., Olšiak, R., Mlkvik, M. (2014). Observation of development of cavitation damage. *EPJ Web of Conferences*, 67, 02053.

[11] Ternik, P., Rudolf, R. (2013). Laminar natural convection of non-Newtonian nanofluids in a square enclosure with differentially heated side walls. *International Journal of Simulation Modelling*, 12 (1), 5-16.

[12] Sikora, R., Bureček, A., Hružík, L., Vašina, M. (2015). Experimental investigation of cavitation in pump inlet. *EPJ Web of Conferences*, 92, 02081.

[13] Jablonská, J., Bojko, M. (2015). Multiphase flow and cavitation - comparison of flow in rectangular and circular nozzle. *EPJ Web of Conferences*, 92, 02028.

[14] Schnerr, G.H., Sauer, J. (2002). Physical and numerical modeling of unsteady cavitation dynamics. In *4th International Conference on Multiphase Flow (ICMF-2001).* Elsevier.

[15] Bureček, A., Hružík, L., Vašina, M. (2015). Determination of undissolved air content in oil by means of compression method. *Strojniški vestnik - Journal of Mechanical Engineering*, 61 (7-8), 477-485.

[16] Bilus, I., Morgut, M., Nobile, E. (2013). Simulation of sheet and cloud cavitation with homogenous transport models. *International Journal of Simulation Modelling*, 12 (2), 94-106

Received August 19, 2017.
Accepted November 13, 2017.

MEASUREMENT SCIENCE REVIEW, **17**, (2017), No. 6, 257-263

DE GRUYTER OPEN

MEASUREMENT SCIENCE REVIEW

Journal homepage: http://www.degruyter.com/view/j/msr

ISSN 1335-8871

Two Methods of Automatic Evaluation of Speech Signal Enhancement Recorded in the Open-Air MRI Environment

Jiří Přibil[1], Anna Přibilová[2], Ivan Frollo[1]

[1]*Institute of Measurement Science, SAS, Dúbravská cesta 9, SK-841 04 Bratislava, Slovakia, Jiri.Pribil@savba.sk*
[2]*Institute of Electronics and Photonics, FEE&IT, SUT, Ilkovičova 3, SK-812 19 Bratislava, Slovakia*

The paper focuses on two methods of evaluation of successfulness of speech signal enhancement recorded in the open-air magnetic resonance imager during phonation for the 3D human vocal tract modeling. The first approach enables to obtain a comparison based on statistical analysis by ANOVA and hypothesis tests. The second method is based on classification by Gaussian mixture models (GMM). The performed experiments have confirmed that the proposed ANOVA and GMM classifiers for automatic evaluation of the speech quality are functional and produce fully comparable results with the standard evaluation based on the listening test method.

Keywords: Acoustic noise suppression, magnetic resonance imaging, speech processing, statistical analysis.

1. INTRODUCTION

Construction of 3D articulatory models is necessary for better representation of the human vocal tract function and the subsequent articulatory speech synthesis. For this reason, the audio signal must be recorded simultaneously with the image scanning [1]. The magnetic resonance imaging (MRI) device is used to obtain the vocal tract images of the articulating person that lies in the scanning area while the MR sequence is running [2], [3]. The MRI equipment consists of a gradient coil system producing three orthogonal linear magnetic fields for spatial scanning. The function of these gradient coils is accompanied by an acoustic noise due to rapidly changing Lorentz forces during fast switching inside the weak static field environment [4]. The speech signal recorded under such conditions may be analyzed only if the adequate signal-to-noise ratio is achieved [5]. Several different methods can be used for reduction of the acoustic noise generated in the MRI scanner [6]-[9]. The problem of processing the speech signal in the presence of noise may be solved by various techniques, e.g., the blind source separation by independent component analysis [10]. In our previous research, the noise reduction method was based on the fact that the mentioned acoustic noise of the MRI machine is a periodic signal with its fundamental frequency that may be filtered and processed in the spectral domain [11]-[12].

Objective or subjective criteria can be used for evaluation of enhancement. The subjective ones are based on auditory evaluation by listeners using various categories, such as the mean opinion score, ABX test for comparison of two speech signals with the third one, recognition of expressive speech, annotation of the speech corpus, etc. [13]). The objective approaches for measuring the speech signal quality [14] comprise, for example, evaluation of differences between the speech spectral envelopes [11] or spectral distances [12], etc. These features may be compared and matched using the statistical approaches, like the analysis of variances (ANOVA) [15], [16] or hypothesis tests [17], [18]. The final evaluation in these approaches bears the form of a recognition score that can be obtained by the methods based on artificial neural networks, the nearest neighbor [19], vector quantization classifiers [20], hidden Markov models [21], and support vector machines (SVM) [22]. However, predominantly, the Gaussian mixture models (GMM) [23] are used. The best results are usually achieved by a fusion of different recognition methods, e.g., combination of GMM with SVM used for speaker recognition in the same way as for language recognition [24].

The paper describes the experiments that use the statistical methods based on the ANOVA analysis and the hypothesis tests and, on the other hand, the GMM-based speech quality classifier. Both approaches are used for automatic evaluation of the speech quality after utilization of three different methods of speech enhancement. The motivation of the work was to find an alternative approach to the standard listening tests. It is important in the cases of small audible (or even indiscernible) differences or when their collective realization is problematic, etc. The main advantage of this system is its automatic functioning without human interaction and the possibility of direct numerical matching of the obtained results using the objective comparison criterion.

DOI: 10.1515/msr-2017-0031

2. METHODS

A. *Noise Suppression in speech signal*

We analyze functionality and successfulness of application of three different methods of the acoustic noise suppression for enhancement of the speech signal recorded during phonation in the MRI environment:

1. The first noise reduction method (further called as *Nsup1*) is based on limitation of the real cepstrum of the noisy speech and clipping the peaks corresponding to the harmonic frequencies of the acoustic noise [11]. This method works well when the basic pitch period of the human voice differs from the repeating period of the running MR scan sequence [12]. In this case, the speech signal with the superimposed noise is recorded by one pick-up microphone.
2. The second tested noise suppression approach (*Nsup2*) uses a subtraction between the short-time spectra of the audio signals recorded by two microphones: the first one recording the speech together with the acoustic noise, the second one recording only the acoustic noise [11].
3. The third method (*Nsup3*) is based on spectral subtraction of the MR scan periodic noise from the same noise superimposed on the speech signal, however, both short-time spectra are estimated from the recording picked-up by the same microphone [12].

The source-filter speech synthesizer with cepstral parameterization of the impulse response of the vocal tract model is used for the reconstruction after the noise suppression in all cases. Each of the applied methods uses different arrangement and practical realization of the recording process as well as the pick-up microphone(s) location [12].

B. *ANOVA-based classification of the speech signal*

The first part of our speech quality evaluation after application of different methods of noise suppression in the speech signal recorded in the environment of the open-air MRI device working with the weak magnetic field is based on the ANOVA analysis. This approach focuses on testing whether there is a common mean of speech features from several groups. Besides the ANOVA *F*-test giving the ratio of variances between and within groups [16], the hypothesis probability resulting from the Wilcoxon test [25] or the Mann-Whitney U test [26] comparing whether two samples come from identical distributions with equal medians or they do not have equal medians, the Ansari-Bradley hypothesis test [27] is used to specify whether two distributions are the same or they differ in their variances. For a chosen significance level the resulting logical value "0" denotes that the null hypothesis cannot be rejected and the value "1" indicates that it can be rejected.

In the developed classification method the speech spectral properties and prosodic parameters extracted from the clean speech are stored in the database DB_{Orig}, from the speech with MRI noise in DB_{Nfonat}, and from the de-noised speech in the databases $DB_{Nsup1..N}$, treated separately for male and female voices. These speech features and parameters are processed by the one-way ANOVA analysis and then the histograms of the occurrences are calculated – see the block diagram in Fig.1. Three comparison methods are used for each of the speech features and the following parameters are determined:

1. absolute distance between group means of the original speech and the speech enhanced by the methods $D_{OT1\text{-}3}$ after the multiple comparison applied to ANOVA statistical results – see visualization in Fig.2.a),
2. hypothesis probability based on the Ansari-Bradley or the Wilcoxon test,
3. relative RMS distance D_{RMSrel} between the histograms of features extracted from the DB_{Orig} and $DB_{Nsup1\text{-}N}$, as documented by an example in Fig.2.b).

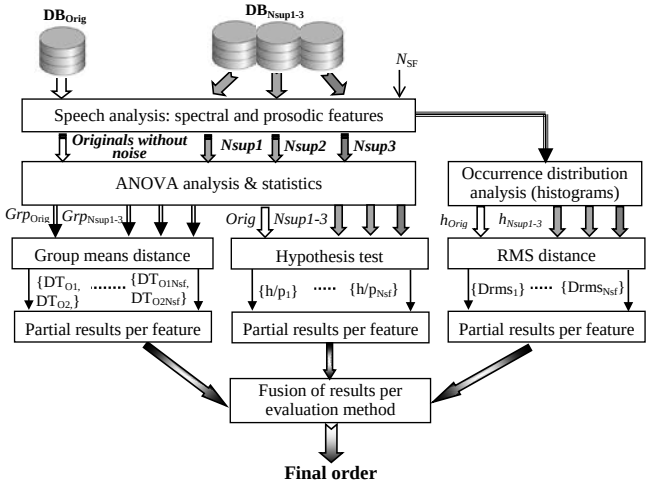

Fig.1. Block diagram of ANOVA-based classifier for evaluation of the enhanced speech signals.

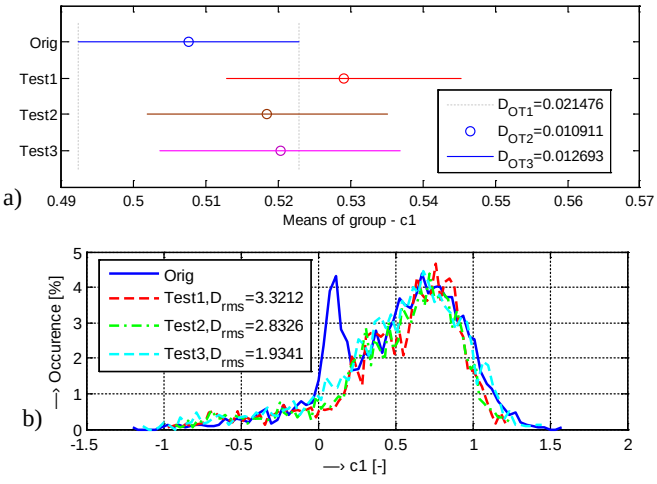

Fig.2. Visualization example of the distance between group means a) and relative RMS distance between the histograms b) for the first cepstral coefficient.

The determined distances and probability values are next sorted by size from minimum (1=nearest to the original) to maximum (3=farthest from the original). From the obtained orders in the range of 1-3 for N_{SF} speech features the histograms of the occurrence distributions are subsequently

calculated for each of the comparison methods (ANOVA/hypothesis test/RMS between histograms) – see the demonstration example in Fig.3. Then, the best order with the maximum occurrence is used for calculation of the final order of mean values for every tested enhanced signal group as the final evaluation value – see the visualization by bar-graphs in Fig.4.

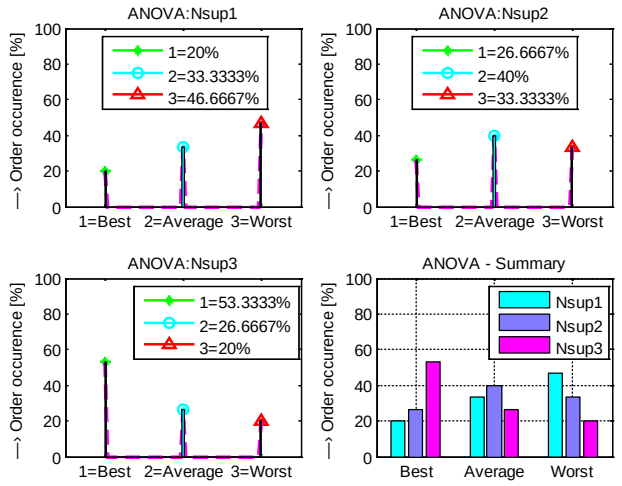

Fig.3. Demonstration example of histograms of order occurences of distances between group means (ANOVA) calculated from all N_{SF} features for three tested noise suppression methods.

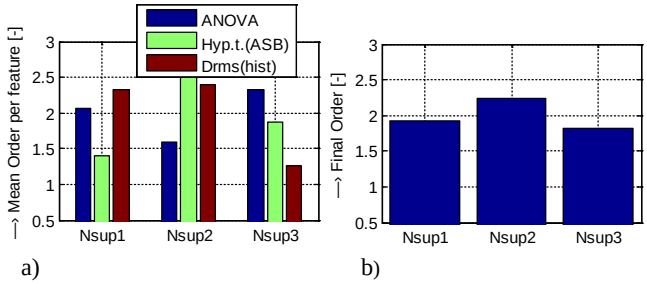

Fig.4. Visualization example of mean values of winner orders per used evalution methods for three tested de-noising approaches a), calculated final order as a result for tested de-noising approaches b).

C. GMM-based evaluation of the speech signal quality

Primarily, the GMMs represent a linear combination of multiple Gaussian probability distribution functions of the input data vector [23]. The covariance matrix and the vector of means together with the weighting parameters have to be determined from the input training data. For the mixture of Gaussians the use of maximum likelihood gives no closed-form analytical solution which would be an ideal case, so the expectation-maximization (EM) iteration algorithm is used for maximizing the likelihood functions [15]. The initial parameters for the EM algorithm are first of all the number of mixtures N_{MIX} and the number of iterations. In general, the elements of the feature vectors could be correlated so that rather a high number of mixture components and a full covariance matrix would be necessary for sufficient approximation. On the other hand, the GMM with a diagonal covariance matrix is usually used in speaker identification [23] due to its lower computational complexity. The GMM classifier returns the probability score that the tested speech signal belongs to the GMM model.

In the standard realization of the GMM classifier, the resulting class is given by the maximum overall probability of all obtained scores (T, n) corresponding to N output classes using the feature vector T from the currently processed speech signal. The main idea of the proposed evaluation method is based on the correlation between the score maxima obtained using the models of the clean speech (further called *Orig*) and the speech with the MRI noise (*Nfonat*). The obtained normalized score values for the enhancement methods *Nsup*1-3 are next ordered using the '*ascend*' sorting for the clean speech models and the '*descend*' sorting for the noisy speech. Finally, the mean score order values in the range of 1-3 (for comparison with the results achieved by the listening tests where "1" represented the best, "2" average, and "3" the worst speech quality) are used for the speech quality evaluation – see an example in Fig.5. The functional block diagram of the whole evaluation method of the speech signal enhancement is shown in Fig.6.

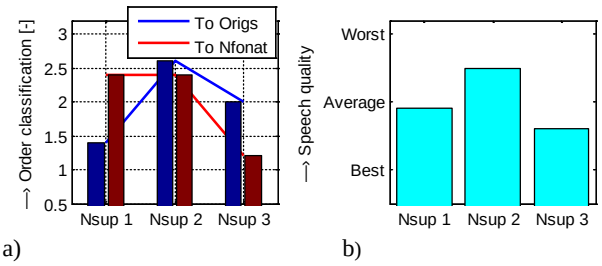

Fig.5. Example of score order determination: partial results for female speaker summarized for all five vowels a), final score as the speech quality evaluation results b).

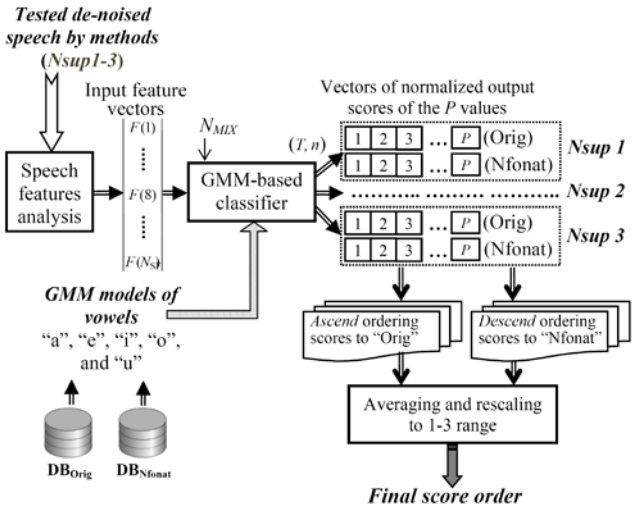

Fig.6. Block diagram of the GMM-based classifier for evaluation of the MRI noise suppression in the speech signal.

D. Determination of features of the speech signal

In the area of the GMM-based speaker [28]-[30], as well as the acoustic signal recognition [31], the most commonly used spectral features are mel-frequency cepstral coefficients together with energy and prosodic parameters. In our experiments the features differ for ANOVA-based evaluation and GMM-based classification of the speech signal quality. The analysis of the input sentence begins with segmentation and determination of the fundamental frequency F0 from the segmented input signal. Next, the smoothed spectral envelope and the power spectral density from the weighted *P* frames of the speech signal are computed for determination of basic and supplementary spectral features. The basic spectral properties are expressed by the statistical parameters as centroid (SC), flatness (SF), spread, skewness, kurtosis, etc. As supplementary spectral features the following parameters are used: spectral decrease (tilt), harmonics-to-noise ratio (HNR), Shannon, Rényi, or Tsallis spectral entropy (SHE/RSE/TSE), etc. For voiced speech description, the first two formant positions F_1, F_2 and their ratio F_1/F_2 are also used in our experiments. The cepstral coefficients $\{c_n\}$ obtained during the process of cepstral analysis, giving information about spectral properties of the human vocal tract, are also successfully used in the feature vectors. The supra-segmental properties include also the speech signal energy expressed by the first cepstral coefficient (En_{c0}) or by the autocorrelation function (En_{r0}). The prosodic parameters consist of two types of energy parameters calculated from the differential microintonation signal $F0_{DIFF}$, zero crossing frequency F_{ZCR}, jitter, and shimmer.

These speech features are stored to different databases depending on the input signal used (DB_{Orig}, DB_{Nfonat}, and $DB_{Nsup1..N}$) – see the block diagram in Fig.7. For the GMM-based experiments, every vector of *P* speech features is subsequently processed to obtain N_{SF} representative statistical values (mean, median, rel. maximum, rel. minimum, etc.).

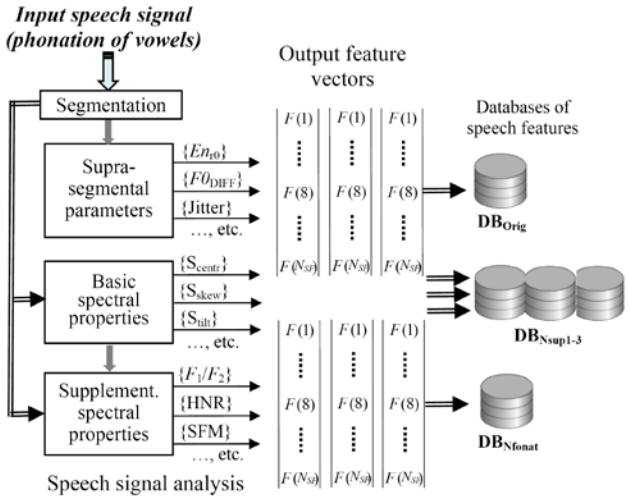

Fig.7. Block diagram of the feature database creation from the speech spectral properties and supra-segmental parameters.

3. MATERIAL AND EXPERIMENTS

A. Speech signal recording and processing

Our experiments were carried out with the open-air MRI equipment E-scan OPERA working with the low magnetic induction of 0.178 Tesla [32]. The speech and noise signals were recorded using the Behringer condenser microphone connected to a separate personal computer via the XENYX 502 mixer and UCA202 audio interface. The audio signals were originally sampled at 32 kHz and then resampled to 16 kHz. The microphone picking up the speech was placed at the position of 150 degrees as documented by the photo of the experimental arrangement in Fig.8. where the tested person lies at 180 degrees. The microphone recording the noise only was placed at 30 degrees. The distance of the microphones from the MRI device central point was 60 cm, and they were situated vertically in the middle between both gradient coils.

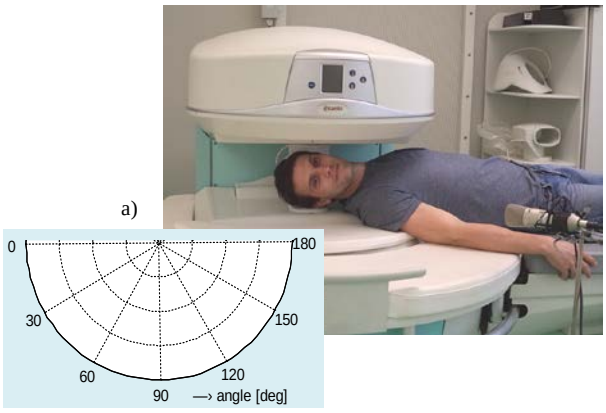

Fig.8. Arrangement of speech and noise recording in the E-scan OPERA: examined person with a pick-up microphone a), principal angle diagram of the MRI scanning area b).

The recorded speech and noise signals were used for creation of the database consisting of five separately phonated long vowels “a”, ”e”, “i”, “o”, and “u” from three male and two female non-professional speakers with time duration interval from 8 to 15 sec. For each of the tested vowels, two types of recordings were carried out. The first one corresponds to the “clean” speech signal of phonation without any MRI noise, only with the superimposed background noise of the temperature stabilizer [12]. The second one is composed of phonation during execution of the MR sequence SSF-3D which is usually applied for MR scanning of the human vocal tract [33].

The input feature vector with the length experimentally set to N_{SF}=16 consisted of a mix of the basic and supplementary spectral and prosodic features. For the ANOVA-based evaluation experiment, the following speech features were used: {En_{c0}, En_{r0}, tilt, SC, flatness, HNR, SHE, RSE, TSE, c_1 – c_3, $F0_{DIFF}$, $F0_{ZCR}$, jitter, and shimmer}. In the case of GMM training and classification the input vector contained statistical representative values of the supra-segmental parameters {$F0_{DIFF}$, jitter, and shimmer}, the basic spectral features determined from the spectral envelopes {F_1/F_2, SC,

tilt}, and the supplementary spectral parameters {HNR, flatness, SHE}.

The Ansari-Bradley hypothesis test was finally used in the ANOVA-based evaluation experiment due to higher consistency of the produced probability results with the absolute distances between group means. In the GMM-based evaluation experiment, a simple diagonal covariance matrix of the GMM as well as the number of mixtures N_{MIX}=8 were finally applied because of their lower computational complexity and relatively good final discriminability of the summary results for all three evaluated methods.

The described analysis and processing of the speech and noise signals were currently realized in the Matlab environment (ver. 2012a), using especially the "Signal Processing" and "Statistics" toolboxes. The Ian T. Nabney "Netlab" pattern analysis toolbox [34] was used for implementation of basic functions for the proposed GMM classifier.

B. Performed evaluation experiments

The subjective evaluation was carried out by the listening test called "*Evaluation of better sound after MRI noise suppression*" by means of the automated internet application located at http://www.lef.um.savba.sk/scripts/itstposl2.dll [35]. This listening test had been accessed by twenty nine listeners in the time period from February 1 to 28, 2017. Our listening test experiment consisted of 10 evaluation sets, each comprising 5 long vowel utterances by male and female voices selected randomly from the speech corpus, so 30 recordings were evaluated in total. For each of the vowel recordings the listener had to choose from four possibilities: "*sounds best*", "*sounds average*", "*sounds worst*" or "*cannot be determined*" – see an example of a screenshot of the listening test in Fig.9. The results obtained in this way are presented in Fig.10.

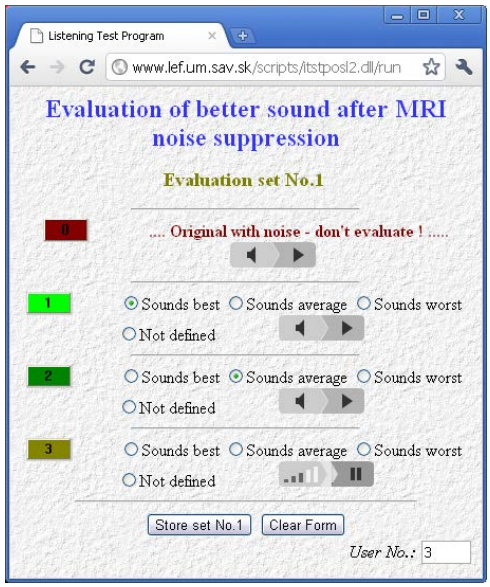

Fig.9. Example of a screen shot of the internet server realization of the listening test; first evaluation set, the first two samples already evaluated, the third one currently playing.

The two basic experiments were focused on verifying the functionality of the developed ANOVA and GMM speech quality classifiers. This step was accompanied by the detailed analysis of the noise suppression method and the speaker type (male/female) – see the partial results in Fig.11. and Fig.12. Finally, the overall obtained values (for all processed vowels and speakers) are matched with the results achieved by the standard listening test method – see Table 2.

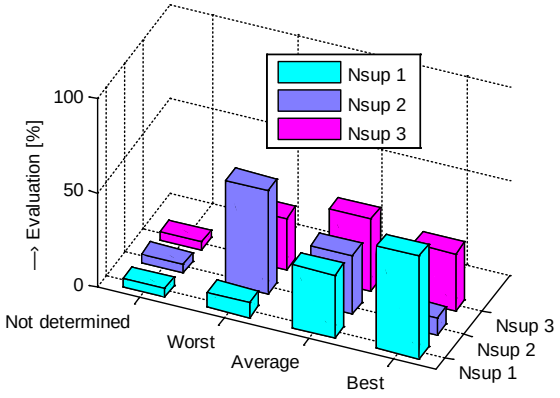

Fig.10. 3D visualization of the evaluation results obtained by the listening test method.

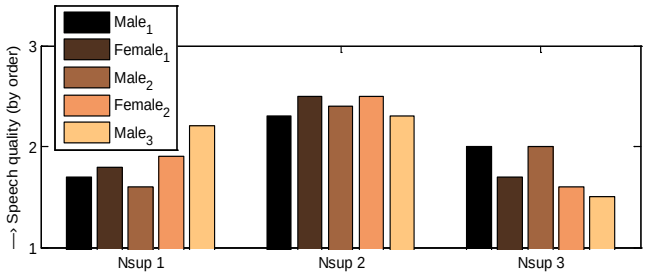

Fig.11. Bar-graph comparison of the final order obtained by the ANOVA evaluation aproach for each of the five tested speakers.

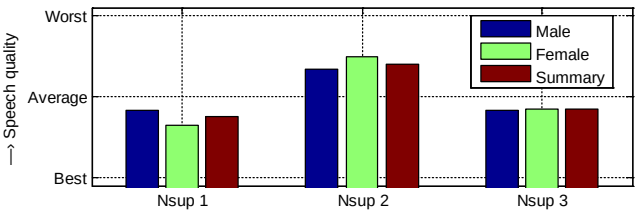

Fig.12. The bar-graph comparison of the GMM-based automatic evaluation results separately for male, female, and both genders of tested speakers, summarized for all five vowels.

Table 2. Final numerical comparison of obtained evaluation orders rescaled to the range of 1-3 (1="*best*", 2="*average*", 3="*worst*").

Method	**Nsup1**	**Nsup2**	**Nsup3**
Listening test	1.52	2.48	1.97
ANOVA-based	1.87	2.34	2.09
GMM-based	1.76	2.41	1.84

4. Conclusion

The performed experiments have confirmed that both proposed automatic classifiers based on statistical approach work correctly and produce results comparable with those attained by the standard listening tests. It was verified on the speech material after the MRI noise suppression consisting of the records of the five basic vowels from five voluntary persons examined in the open-air MRI device during the 3D scanning of human vocal tract.

As documented by the obtained results, the applied setting of the basic parameters for ANOVA and GMM evaluation approaches produces variability of the results for the male/female speakers (see the obtained scores in Fig.11.). On the other hand, the analysis of dependence of the obtained results on different types and different numbers of speech parameters used in the input feature vectors must also be performed. Finally, the computation complexity analysis of the current realization in the Matlab environment revealed that optimization and implementation in a higher programing language is necessary for real-time processing and classification.

Acknowledgment

This work was supported by the Slovak Scientific Grant Agency project VEGA 2/0001/17, the Ministry of Education, Science, Research, and Sports of the Slovak Republic VEGA 1/0905/17, and within the project of the Slovak Research and Development Agency Nr. APVV-15-0029.

The authors would also like to express thanks to all the people who participated in the listening test.

References

[1] Wei, J., Liu, J., Fang, Q., Lu, W., Dang, J., Honda, K. (2016). A novel method for constructing 3D geometric articulatory models. *Journal of Signal Processing Systems*, 82, 295-302.

[2] Aalto, D., Aaltonen, O., Happonen, R.-P. et al. (2014). Large scale data acquisition of simultaneous MRI and speech. *Applied Acoustics*, 83, 64-75.

[3] Kuorti, J., Malinen, J., Ojalammi, A. (2018). Post-processing speech recordings during MRI. *Biomedical Signal Processing and Control*, 39, 11-22.

[4] Tomasi, D., Ernst, T. (2006). A simple theory for vibration of MRI gradient coils. *Brazilian Journal of Physics*, 36, 34-39.

[5] Burdumy, M., Traser, L., Richter, B. et al. (2015). Acceleration of MRI of the vocal tract provides additional insight into articulator modifications. *Journal of Magnetic Resonance Imaging*, 42, 925-935.

[6] Lee, N., Park, Y., Lee, G.W. (2017). Frequency-domain active noise control for magnetic resonance imaging acoustic noise. *Applied Acoustics*, 118, 30-38.

[7] Wu, Z., Kim, Y.C., Khoo, M.C.K., Nayak, K.S. (2014). Evaluation of an independent linear model for acoustic noise on a conventional MRI scanner and implications for acoustic noise reduction. *Magnetic Resonance in Medicine*, 71, 1613-1620.

[8] Oveisi, A., Nestorović, T. (2016). Mu-synthesis based active robust vibration control of an MRI inlet. *Facta Universitatis, Series: Mechanical Engineering*, 14 (1), 37-53.

[9] Sun, G., Li, M., Rudd, B.W. et al. (2015). Adaptive speech enhancement using directional microphone in a 4-T scanner. *Magnetic Resonance Materials in Physics, Biology and Medicine*, 28, 473-484.

[10] Patil, D., Das, N., Routray, A. (2011). Implementation of Fast-ICA: A performance based comparison between floating point and fixed point DSP platform. *Measurement Science Review*, 11 (4), 118-124.

[11] Přibil, J., Horáček, J., Horák, P. (2011). Two methods of mechanical noise reduction of recorded speech during phonation in an MRI device. *Measurement Science Review*, 11 (3), 92-98.

[12] Přibil, J., Přibilová, A., Frollo, I. (2016). Analysis of acoustic noise and its suppression in speech recorded during scanning in the open-air MRI. In *Advances in Noise Analysis, Mitigation and Contro*l. Rijeka, Croatia: InTech, 205-228.

[13] Grůber, M., Matoušek, J. (2010). Listening-test-based annotation of communicative functions for expressive speech synthesis. In *Text, Speech, and Dialogue (TSD) 2010*, LNCS 6231, Springer, 283-290.

[14] Sen, D., Lu, W. (2017). Systems and methods for measuring speech signal quality. *US Patent 9679555*.

[15] Rencher, A.C., Schaalje, G.B. (2008). *Linear Models in Statistics, Second Edition*. John Wiley & Sons.

[16] Lee, C.Y., Lee, Z.J. (2012). A novel algorithm applied to classify unbalanced data. *Applied Soft Computing*, 12, 2481-2485.

[17] Mizushima, T. (2000). Multisample tests for scale based on kernel density estimation. *Statistics & Probability Letters*, 49, 81-91.

[18] Altman, D.G., Machin, D., Bryant, T.N., Gardner, M.J. (2000). *Statistics with Confidence: Confidence Intervals and Statistical Guidelines, 2nd edition*. London: BMJ Books.

[19] Glowacz, A., Glowacz, Z. (2017). Diagnosis of stator faults of the single-phase induction motor using acoustic signals. *Applied Acousticss*, 117, 20-27.

[20] Bapat, O.A., Fastow, R.M., Olson, J. (2013). Acoustic coprocessor for HMM based embedded speech recognition systems. *IEEE Transactions on Consumer Electronics*, 59 (3), 629-633.

[21] Bhardwaj, S., Srivastava, S., Hanmandlu, M., Gupta, J.R.P. (2013). GFM-based methods for speaker identification. *IEEE Transaction on Cybernetics*, 43 (3), 1047-1058.

[22] Vít, J., Matoušek, J. (2013). Concatenation artifact detection trained from listeners evaluations. In *Text, Speech and Dialogue 2013*, LNAI 8082, Springer, 169-176.

[23] Reynolds, D.A., Rose, R.C. (1995). Robust text-independent speaker identification using Gaussian mixture speaker models. *IEEE Transactions on Speech and Audio Processing*, 3, 72-83.

[24] Campbell, W.M., Campbell, J.P., Reynolds, D.A., Singer, E., Torres-Carrasquillo, P.A. (2006). Support vector machines for speaker and language recognition. *Computer Speech and Language*, 20 (2-3), 210-229.

[25] Rodellar-Biarge, V., Palacios-Alonso, D., Nieto-Lluis, V., Gómez-Vilda, P. (2015). Towards the search of detection in speech-relevant features for stress. *Expert Systems*, 32 (6), 710-718.

[26] Mekyska, J., Janousova, E., Gomez-Vilda, P. et al. (2015). Robust and complex approach of pathological speech signal analysis. *Neurocomputing*, 167, 94-111.

[27] Bishop, C.M. (2006). *Pattern Recognition and Machine Learning*. Springer.

[28] Venturini, A., Zao, L., Coelho, R. (2014). On speech features fusion, α-integration Gaussian modeling and multi-style training for noise robust speaker classification. *IEEE/ACM Transactions on Audio, Speech, and Language Processing*, 22 (12), 1951-1964.

[29] Chakroun, R., Zouari, L.B., Frikha, M. (2016). An improved approach for text-independent speaker recognition. *International Journal of Advanced Computer Science and Applications*, 7 (8), 343-348.

[30] Sharma, R., Prasanna, S.R.M., Bhukya, R.K., Das, R.K. (2017). Analysis of the intrinsic mode functions for speaker information. *Speech Communication*, 91, 1-16.

[31] Glowacz, A. (2015) Recognition of acoustic signals of synchronous motors with the use of MoFS and selected classifiers. *Measurement Science Review*, 15 (4), 167-175.

[32] Esaote S.p.A. (2008). *E-scan Opera. Image Quality and Sequences Manual*. 830023522 Rev. A.

[33] Přibil, J., Gogola, D., Dermek, T., Frollo, I. (2012). Design, realization and experiments with a new RF head probe coil for human vocal tract imaging in an NMR device. *Measurement Science Review*, 12 (3), 98-103.

[34] Nabney, I.T. (2004). *Netlab Pattern Analysis Toolbox, Release 3.3*. http://www.aston.ac.uk/eas/research/groups/ncrg/resources/netlab/downloads.

[35] Přibil, J., Přibilová, A. (2013). Internet application for collective realization of speech evaluation by listening tests. In *Proceedings of the International Conference on Applied Electronics (AE2013)*, Plzeň, Czech Republic, 225-228.

Received July 27, 2017.
Accepted November 12, 2017.

MEASUREMENT SCIENCE REVIEW, **17**, (2017), No. 6, 264-268

DE GRUYTER OPEN

MEASUREMENT SCIENCE REVIEW

Journal homepage: http://www.degruyter.com/view/j/msr

ISSN 1335-8871

Optimization of Nano-Grating Pitch Evaluation Method Based on Line Edge Roughness Analysis

Jie Chen[1], Jie Liu[1], Xingrui Wang[1], Longfei Zhang[1], Xiao Deng[2], Xinbin Cheng[1], Tongbao Li[1]

[1]*Institute of Precision Optical Engineering, School of Physics Science and Engineering, Tongji University, 200092, Shanghai, China*
[2]*School of Aerospace Engineering and Applied Mechanics, Tongji University, 200092, Shanghai, China*
Corresponding author: Xiao Deng, Email: 1110490dengxiao@tongji.edu.cn

Pitch uncertainty and line edge roughness are among the critical quality attributes of a pitch standard and normally the analyses of these two parameters are separate. The analysis of self-traceable Cr atom lithography nano-gratings shows a positive relevance and sensitivity between LER and evaluated standard deviation of pitch. Therefore, LER can be used as an aided pre-evaluation parameter for the pitch calculation method, such as the gravity center method or the zero-crossing points method. The optimization of the nano-grating evaluation method helps to obtain the accurate pitch value with fewer measurements and provide a comprehensive characterization of pitch standards.

Keywords: Pitch evaluation, nano-grating standard, line edge roughness, atomic force microscope.

1. INTRODUCTION

Lateral pitch standards, such as one-dimensional or two dimensional nano-gratings, are widely used as transfer standards to calibrate the nonlinearity or image magnification for all kinds of microscopes [1]. Many nanofabrication methods have been utilized to fabricate lateral pitch structures, including e-beam lithography, multilayer gratings [2], [3], atom lithography [4]-[6], atom-based rulers [7]-[9], and so on. Before the nanoscale pitch structures can be used as transfer standards, pitch uncertainties need to be measured with metrological AFMs and estimated with the effective pitch evaluation methods [10].

Effective pitch evaluation method is one of the key factors to lower the calculated pitch uncertainty, thereby increasing the calibration accuracy [11], [12]. The Gravity Center (GC) method [1], [13], [14], Zero Cross Points (ZCP) method [11] and Fourier Transform (FT) method [1], [15], [16] are the most commonly used pitch evaluation methods for one/two dimensional nano-grating standards. As a kind of pitch calculation method based on the real nano-grating profiles, the uncertainty of measurement results with GC or ZCP method relies on the selection of effective profiles. Therefore, optimization of effective profile selection for GC or ZCP methods offers a new way to increase the calibration accuracy of pitch standards.

Normally, line edge roughness (LER) refers to the randomly varied edges of critical dimensions (CD) of grate patterns [17]. Previous study has noted the importance of LER as a critical quality attribute of the pitch: a reference line with lower LER can achieve the same accuracy with fewer measurements [18]. Motivated by this concept, in this paper, we have introduced LER as a reference evaluation parameter for the pitch evaluation of one-dimensional self-traceable Cr atom lithography nano-gratings. The analysis shows that there is a positive correlation between LER and evaluated standard deviation of pitch of AFM measurement data, which provides key evidence for the effective profile selection during the pitch evaluation process and further increases the pitch calibration accuracy.

2. THEORIES

A. Pitch evaluation method with LER

Two profile-based methods are utilized in this paper: GC method and ZCP method, which are illustrated in Fig.1.a). First, a threshold line is set to divide the nano-grating profiles into two parts. For the GC method [1], [11]-[13], the geometrical center above the threshold line is treated as the gravity center; the distance of two neighboring gravity centers is defined as the pitch. For the ZCP method [11], [12], zero cross points are the intersection points between the threshold line and profile curves of the nano-grating pattern. The middle point of a pair of zero crossing points on each nano-grating pattern is treated as the geometric center point. Then the pitch values of the ZCP method are defined as the distance between neighboring middle points.

The profile cutting proportion (p), which is the profile below the threshold line, plays a critical role in pitch uncertainty estimation. Generally, the profile cutting

DOI: 10.1515/msr-2017-0032

proportion is set to be 50 % of the peak to valley height (PTVH) as a tradition, but whether 50 % is the best or not has not been elucidated clearly yet. If we expand the threshold line to a plane at the same height, then we get intersecting lines along the nano-grating edges, as demonstrated in Fig.1.b).

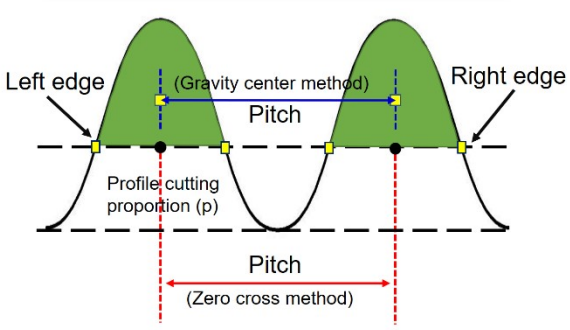

a)

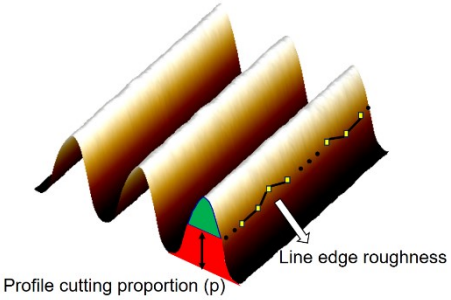

b)

Fig.1. a) Schematic of the Gravity Center method and the Zero Cross Method; b) Definition of line edge roughness of Cr atom lithography nano-gratings.

The LER describes the variation of the crossing points, which will provide effective information to select the best profile cutting proportion and, thereby, minimize the evaluated standard deviation of pitch. The average edge and the standard deviation (σ) of the line edge are defined as follows [18]:

$$\begin{cases} \bar{x} = \dfrac{\left(\sum_{i=1}^{N} x_i\right)}{N} \\ 3\sigma = 3\sqrt{\dfrac{\sum_{i=1}^{N} \Delta x_i^2}{N-1}} = 3\sqrt{\dfrac{\sum_{i=1}^{N} (x_i - \bar{x})^2}{N-1}} \end{cases} \quad (1)$$

Where X_i is the position measured of the *i*th point along the line edge. Normally, LER must be reported as 3 σ of the total, and in our case, we will investigate the LER of both edges over a length of L, and every time L is divided into 20 spacings apart. Then we obtained 21 measured positions to calculate the LER. The length L is assigned to be 0.5P, 1P, 2P, 3P, 4P, respectively, where P is the nominal pitch (212.8 nm).

B. Cr atom lithography nano-gratings

The nano-gratings used here are fabricated by laser focused Cr atomic deposition [4], [5], [19], i.e., the so-called Cr atom lithography nano-gratings. The detail experimental setup is described elsewhere [20], [21]. During the Cr nano-grating fabrication process, collimated Cr atoms are focused to the nodes or antinodes of a standing wave grazing across the substrate surface. So, the period of the Cr nano-gratings (212.8 nm) is directly traceable to the half of the laser light wavelength, which is strictly locked to specified atomic level transitions. In this way, the Cr atom lithography nano-gratings can be used as self-traceable calibration length standard in nanotechnology.

The profile of Cr nano-gratings has an advantage of reducing the image distortion caused by the tip effect, which offers great convenience for the LER analysis. The images obtained by the AFM normally are a combination of tip geometry and sample surface. The linewidth is normally broadened due to the resulting dilation of the tip. Fig.2.a) is the cross section TEM image of Cr atom lithography nano-gratings, the height to width ratio is relatively low, so the measured profile can reduce the tip effect and reveal the real profile to the full extent, as illustrated in Fig.2.b).

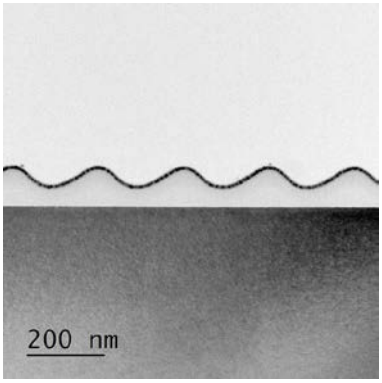

a)

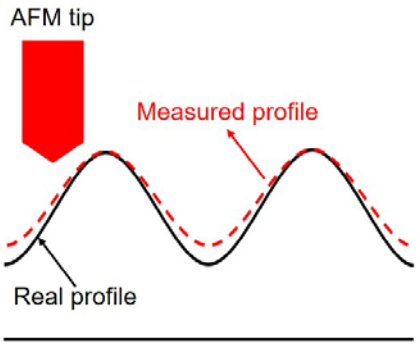

b)

Fig.2. a) Cross section TEM image of Cr nano-gratings; b) The discrepancy between measured profile and real profile of AFM measurement for Cr nano-gratings.

3. LINE EDGE ROUGHNESS ANALYSIS

A. Line edge roughness of Cr nano-gratings

Fig..3 shows the AFM image and grating profile of Cr nano-gratings used for the line edge roughness analysis. The selected PTVH is around 50 nm with very smooth and uniform parallel lines in Fig.3.a) and Fig.3.b). The original pixel size of the image is 488×450, we did the data interpolation and low pass filter to eliminate the imaging noise [1]. As mentioned before, the LER is calculated over left and right edges of a length L which is divided into 20 spacings apart (Fig.3.a)). The LER analysis results of this AFM image are typical and representative in similar image calculations.

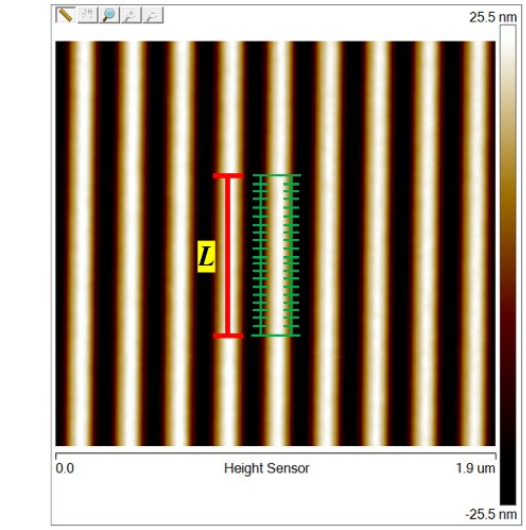

a)

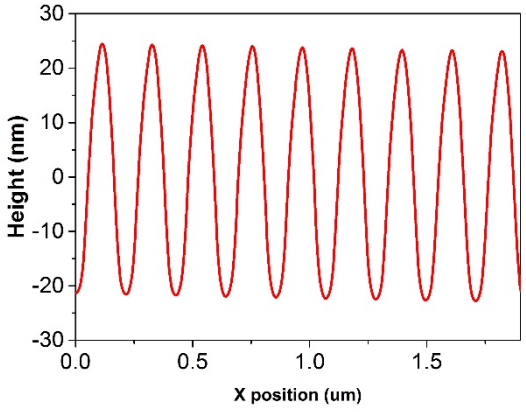

b)

Fig.3. a) AFM image of Cr nano-gratings (1.9 μm×1.75 μm); b) AFM profile of Cr nano-gratings with a peak to valley height of around 50 nm.

Fig.4.a) shows the 3 σ LER of left and right edges as a function of profile cutting proportion (p), and the calculation length L of the LER is P (212.8 nm). Here the profile cutting proportion (p) is the profile below the threshold line in Fig.1.a). It is obvious that the LER keeps at a very low level (below 1 nm) when p ranges from 0.2 to 0.6 and the minimum LER appears at p=0.3 of these discrete value assignments, which verified the speculation about the best p selection. The LER will increase when p decreases to 0.1 due to increased randomness of the laser focused Cr structures at the top. The same trend appears when p increases to 0.9, together with the increased discrepancy between left LER and right LER, which are highly possibly caused by the AFM scanning distortion induced by the tip effect. In addition, it should be noted that the LER of p<0.5 of left and right edges are almost identical even with a slightly asymmetric structure, which may be an evidence to explain why the self-traceable Cr nano-gratings have an advantage of low uncertainty.

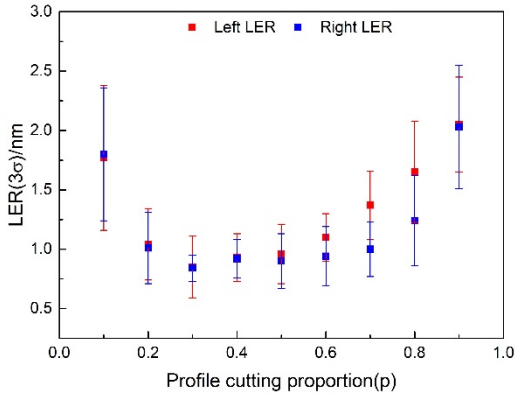

a)

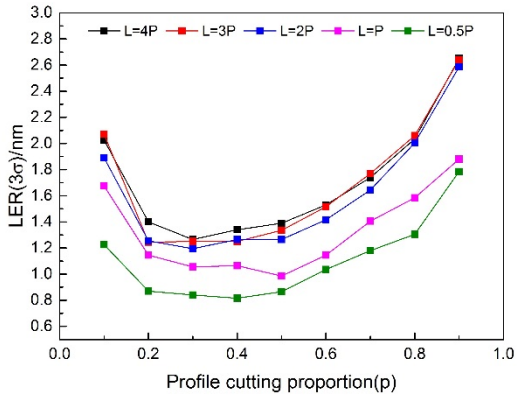

b)

Fig.4. a) Left and Right LER as a function of profile cutting proportion; b) Average LER as a function of profile cutting proportion over different calculation length (0.5P~4P).

Fig.4.b) demonstrates the average LER of left and right edges as a function of profile cutting proportion over different calculation length ranging from 0.5P to 4P. The similar distribution phenomenon shows up over different calculation length in Fig.4.a). As the calculation length increases from 0.5P to 2P, the average LER rises gradually; but after the length exceeds 2P to 4P, the average LER keeps stable without obvious increase. This indicates that a calculation length of 2P (425.6 nm) is long enough to evaluate the maximum LER level of the laser focused Cr atomic nano-gratings.

B. The relationship between line edge roughness and evaluated standard deviation of pitch

Next, we examined the relationship between lined edge roughness and the evaluated standard deviation of pitch. The AFM images we calculated were acquired by a commercial AFM (Bruker, Dimension Edge), which is non-metrological. As we introduced in the context, the Cr atom lithography nano-grating used here is self-traceable, its pitch is expected to be 212.8 nm. Jabez. J. McClelland has even examined the average pitch of Cr nano-gratings by optical diffraction method, which turned out to be 212.7777±0.0069 nm, with a relative uncertainty of a few times 10^{-5} [22]. Therefore, we corrected the calculated average pitch to 212.8 nm and got the evaluated standard deviation of pitch by a correction coefficient.

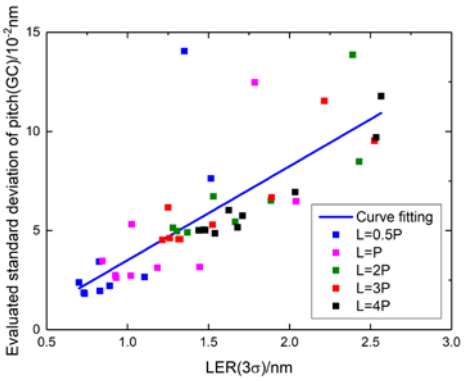

a)

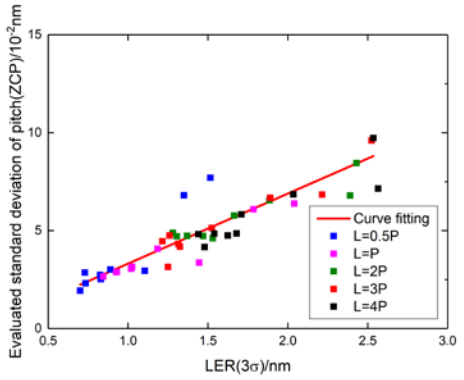

b)

Fig.5. Relationship between LER with evaluated standard deviations of pitch calculated by a) Gravity center method; b) Zero cross points method.

Fig.5. shows the corresponding evaluated standard deviations of pitch under every LER condition over different calculation lengths varying from 0.5P to 4P. Fig.5.a) and Fig.5.b) are the results of the gravity center method and the zero-crossing points method, respectively. From both figures, it is obvious that there is a positive correlation between LER and evaluated standard deviation of pitch, and the relationship tends to be linear. Compared with the ZCP method, the sensitivity scale of evaluated standard deviation of pitch on LER based on the GC method is a little bit higher. The reason for this discrepancy is the difference between GC and ZCP method. In the ZCP method, only the LER information at the reference line are involved in the pitch calculation, while in the GC method all the LER information above the reference line are contained inside. Though some of the lined edge randomness is neutralized because of the nano-gratings' symmetry, the top part of the nano-grating (for example, 10 % of the top profile) has lower symmetry and higher LER as demonstrated in Fig.4.a). The relationship of LER and evaluated standard deviation of pitch determines that LER can be used as an aided pre-evaluated parameter for the pitch evaluation method, which offers a more comprehensive evaluation result for the pitch standards.

C. Pitch evaluation method optimization

The fundamental pitch distance, the pitch uniformity, the quality of the LER and the accuracy of the certified pitch value, and the traceability are the most critical qualities which attribute a pitch standard [18]. From the analysis of self-traceable Cr nano-gratings, there is a strong positive correlation between LER and evaluated standard deviation of pitch. Based on the relevance of these two parameters, it is suggested to introduce LER calculation as an aided pre-evaluation parameter for the pitch calculation method, especially for best profile cutting proportion selection during GC or ZCP method. This not only helps to obtain the accurate pitch value with fewer averaging sample measurements, but also helps to extract more accurate pitch evaluation information with the same experimental data. At the same time, together with evaluated standard deviation of pitch, LER analysis offers a comprehensive evaluation about the critical qualities of a pitch, such as the accuracy and the uniformity characteristics.

4. Conclusions

In this paper, a LER analysis of self-traceable Cr nano-gratings was conducted to show the relevance between the LER and evaluated standard deviation of pitch in the pitch evaluation method (i.e. gravity center method and zero cross points method). The results demonstrate a positive correlation between LER and the evaluated standard deviation of pitch, which indicates that LER can be used as an aided pre-evaluation parameter for pitch calculation method, especially for effective profile cutting proportion selection for GC or ZCP method. The optimization of the nano-grating pitch evaluation method based on LER would offer convenience to obtain the accurate pitch value with fewer measurements and provide a comprehensive evaluation about the critical qualities of pitch standards.

Acknowledgement

This work is supported by National Natural Science Foundation of China (Grant No. 51475335, 51705369), National Key Research and Development Program of China (Grant No.2016YFA0200902), National Key Scientific Instrument and Equipment Development Projects of China (No.2014YQ090709) and China Postdoctoral Science Foundation (No.2017M611613).

REFERENCES

[1] Dai, G., Koenders, L., Pohlenz, F., Dziomba, T., Danzebrink, H. (2005). Accurate and traceable calibration of one-dimensional gratings. *Measurement Science and Technology*, 16 (6), 1241-1249.

[2] Misumi, I., Dai, G., Lu, M., Sato, O., Sugawara, K., Gonda, S., Takatsuji, T., Danzebrink, H., Koenders, L. (2010). Bilateral comparison of 25 nm pitch nanometric lateral scales for metrological scanning probe microscopes. *Measurement Science and Technology*, 21 (3), 035105.

[3] Xingrui, W., Zhao, Y., Liu, J., Chen, J., Li, T., Xinbin, C. (2016). Fabrication and characterization of one-dimensional multilayer gratings for nanoscale microscope calibration. In *Nanoengineering: Fabrication, Properties, Optics and Devices XIII*, 28-31 August 2016, San Diego, US. SPIE 9927.

[4] McClelland, J., Scholten, R., Palm, E., Celotta, R. (1993). Laser-focused atomic deposition. *Science*, 262 (5135), 877-880.

[5] Celotta, R., McClelland, J. (1994). *Method of fabricating laser controlled nanolithography*. Patent US5360764 A.

[6] Xiao, D., Tongbao, L., Lihua, L., Yan, M., Rui, M., Junjing, W., Yuan, L. (2014). Fabrication and measurement of traceable pitch standard with a big area at trans-scale. *Chinese Physics B*, 23 (9), 143-147.

[7] Dai, G., Heidelmann, M., Kübel, C., Prang, R., Fluegge, J., Bosse, H. (2013). Reference nano-dimensional metrology by scanning transmission electron microscopy. *Measurement Science and Technology*, 24 (8), 085001.

[8] Li, K. (2011). *Nanofabrication on engineered silicon (100) surfaces using scanning probe microscopy*. Unpublished doctoral dissertation, University of Maryland, US.

[9] Ballard, J.B., Dick, D.D., McDonnell, S.J., Bischof, M., Fu, J., Owen, J.H., Owen, W.R., Alexander, J.D., Jaeger, D.L., Namboodiri, P. (2015). Atomically traceable nanostructure fabrication. *Journal of Visualized Experiments Jove*, 101, e52900.

[10] Korpelainen, V. (2014). *Traceability for nanometre scale measurements: Atomic force microscopes in dimensional nanometrology*. Unpublished doctoral dissertation, University of Helsinki, Finland.

[11] Huang, Q., Gonda, S., Misumi, I., Keem, T., Kurosawa, T. (2006). Research on pitch analysis methods for calibration of one-dimensional grating standard based on nanometrological AFM. In *Third International Symposium on Precision Mechanical Measurements*, 2-5 August 2006, Urumqi, China. SPIE 6280.

[12] Huang, Q., Misumi, I., Gonda, S., Sato, O., Kurosawa, T. (2006). Pitch calibration of one-dimensional grating standard by tapping mode nanometrological atomic force microscope. In *Sixth International Symposium on Instrumentation and Control Technology: Signal Analysis, Measurement Theory, Photo-Electronic technology, and Artificial Intelligence*, 13-16 October 2006, Beijing, China. SPIE 6357.

[13] Misumi, I., Gonda, S., Kurosawa, T., Takamasu, K. (2003). Uncertainty in pitch measurements of one-dimensional grating standards using a nanometrological atomic force microscope. *Measurement Science and Technology*, 14 (4), 463-471.

[14] Dai, G., Pohlenz, F., Dziomba, T., Xu, M., Diener, A., Koenders, L., Danzebrink, H. (2007). Accurate and traceable calibration of two-dimensional gratings. *Measurement Science and Technology*, 18 (2), 415-421.

[15] Li, C., Yang, S., Wang, C., Jiang, Z. (2016). EEMD based pitch evaluation method for accurate grating measurement by AFM. *Applied Surface Science*, 380, 274-280.

[16] Chen, X., Koenders, L. (2014). A novel pitch evaluation of one-dimensional gratings based on a cross-correlation filter. *Measurement Science and Technology*, 25 (4), 044007.

[17] Shin, C. (2016). *Variation-Aware Advanced CMOS Devices and SRAM*. Springer, 56.

[18] Tortonese, M., Prochazka, J., Konicek, P., Schneir, J., Smith, I.R. (2002). 100-nm-pitch standard characterization for metrology applications. In *Metrology, Inspection, and Process Control for Microlithography XVI*, 3-6 March 2002, Santa Clara, Canada. SPIE 4689, 558-564.

[19] Lihua, L., Yuan, L., Xiao, D., Guofang, F., Xiaoyu, C., Xinbin, C., Junjing, W., Gang, L., Tongbao, L. (2015). Laser-focused Cr atomic deposition pitch standard as a reference standard. *Sensors and Actuators A: Physical*, 222, 184-193.

[20] Xiao, D., Yan, M., Pingping, Z., Wanjing, Z., Sheng, C., Shengwei, X., Tongbao, L. (2012). Investigation of shadow effect in laser-focused atomic deposition. *Applied Surface Science*, 261, 464-469.

[21] Lihua, L., Yuan, L., Guofang, F., Junjing, W., Xiao, D., Xiaoyu, C., Tongbao, L. (2014). Nano-traceability study of a Cr standard grating fabricated by laser-focused atomic deposition. *Chinese Physics Letters*, 31 (7), 46-49.

[22] McClelland, J.J., Anderson, W.R., Bradley, C.C., Walkiewicz, M., Celotta, R.J., Jurdik, E., Deslattes, R.D. (2003). Accuracy of nanoscale pitch standards fabricated by laser-focused atomic deposition. *Journal of Research-National Institute of Standards and Technology*, 108 (2), 99-113.

Received July 30, 2017.
Accepted November 13, 2017.

MEASUREMENT SCIENCE REVIEW, **17**, (2017), No. 6, 269-272

DE GRUYTER OPEN

MEASUREMENT SCIENCE REVIEW

Journal homepage: http://www.degruyter.com/view/j/msr

ISSN 1335-8871

Verification of the Indicating Measuring Instruments Taking into Account their Instrumental Measurement Uncertainty

Igor Zakharov[1], Pavel Neyezhmakov[2], Olesia Botsiura[3]

[1] *Kharkiv National University of Radio Electronics, Department of Metrology and Technical Expertise, Faculty of Infocommunications, University, Nauky Ave., 14, 61166, Kharkiv, Ukraine, newzip@ukr.net*
[2] *National Scientific Centre "Institute of Metrology", Myronosytska Str., 42, 61002, Kharkiv, Ukraine, pavel.neyezhmakov@metrology.kharkov.ua*
[3] *Kharkiv National University of Radio Electronics, Department of Higher Mathematics, Faculty of Information-Analytical Technologies and Management, University, Nauky Ave., 14, 61166, Kharkiv, Ukraine*

The specific features of the measuring instruments verification based on the results of their calibration are considered. It is noted that, in contrast to the verification procedure used in the legal metrology, the verification procedure for calibrated measuring instruments has to take into account the uncertainty of measurements into account. In this regard, a large number of measuring instruments, considered as those that are in compliance after verification in the legal metrology, turns out to be not in compliance after calibration. In this case, it is necessary to evaluate the probability of compliance of indicating measuring instruments. The procedure of compliance probability determination on the basis of the Monte Carlo method is considered. An example of calibration of a Vernier caliper is given.

Keywords: Probability of compliance; uncertainty of measurement; calibration; verification; uncertainty budget; maximum permissible error.

1. INTRODUCTION

The items 5.6.2.1.1 and 5.10.4.1.b of ISO 17025:2005 [1] prescribe that calibration certificates for measuring instruments (MIs) shall contain "the measurement results, including the measurement uncertainty and/or a statement of compliance with an identified metrological specification". From this requirement, it follows that the presence of an indication of conformity of the calibrated MI to the established metrological requirements or separate metrological characteristics is necessary in the calibration certificate. The conformity assessment of the gauge according to the specified requirements is considered in a number of documents [2]-[8]. The main requirement of these documents is the need to take into account the uncertainty of measurement when performing conformity assessment.

2. SUBJECT & METHODS

2.1. Conformity region and probability of compliance

Conformity with a specification is proved when the complete measurement result falls within the tolerance region [5]:

$$LSL \le y - U \text{ or } y + U \le USL ,$$

where *LSL* and *USL* – the lower and upper specification limits of the tolerance region, respectively; y and U – the estimate of measurand and expanded uncertainty, respectively.

These expressions are combined into one, in which the measurement result is within the conformity region [5]:

$$LSL + U \le y \le USL - U . \quad (1)$$

A measuring instrument may be an indicating measuring instrument (IMI) or a material measure. The measurand of IMI calibration is the systematic error E_x. In verification of an IMI, the modulus of the specification limits of tolerance region is equal to its maximum permissible error (MPE):

$$\left|LSL_{\text{IMI}}\right| = USL_{\text{IMI}} = \text{MPE} .$$

It should be noted that the main sources of uncertainty of IMI calibration are: instrumental uncertainty of the measurement standard, its instability, changes in its operating conditions, mutual influence of the measurement standard and the IMI to be calibrated; the observed variation in the readings of the calibrated IMI; resolution of a displaying device of IMI. With all uncertainty components taken into account, the extended measurement uncertainty during calibration may be greater than MPE.

DOI: 10.1515/msr-2017-0033

In the example S10 of calibration of a Vernier caliper with a resolution of 0.05 mm, considered in [9], the measurement model is:

$$E_X = l_{iX} - l_S + L_S \cdot \overline{\alpha} \cdot \Delta t + \delta l_{iX} + \delta l_M ,$$

where l_{iX} – indication of the caliper; l_S – length of the actual gauge block; L_S – nominal length of the actual gauge block; $\overline{\alpha}$ – average thermal expansion coefficient of the caliper and the gauge block; Δt – difference in temperature between the caliper and the gauge block; δl_{iX} – correction for the finite resolution of the caliper; δl_M – correction for the mechanical effects.

The uncertainty budget is given in Table 1. There are 2 dominating rectangular contributions in this budget. Therefore, the expanded measurement uncertainty (for trapezoidal distribution law) was:

$$U = k \cdot u(E_X) = 1.83 \cdot 0.0325\,\text{mm} \approx 0.06\,\text{mm}.$$

The coverage factor 1.83 for trapezoidal distribution is substituted in clause S10.10 [9].

Table 1. Uncertainty budget of Vernier caliper calibration [9].

quantity X_i	estimate x_i	standard uncertainty $u(x_i)$	probability distribution	sensitivity coefficient c_i	uncertainty contribution $u_i(y)$
l_{iX}	150.10 mm	–	–	–	–
l_S	150.00 mm	0.46 μm	rectangular	-1.0	- 0.46 μm
Δt	0	1.15 K	rectangular	1.7 μmK^{-1}	2.0 μm
δl_{iX}	0	14.4 μm	rectangular	1.0	14.4 μm
δl_M	0	29 μm	rectangular	1.0	29 μm
E_X	0.10 mm	–	–	–	32.44 μm

So, such a Vernier caliper will be unusable even if its readings do not deviate from the value of the end length gauge, since it is usually equal to its resolution for MPE of the Vernier caliper. If we neglect the unjustifiably high uncertainty associated with the influence of the measuring force (this is quite true for the Vernier calipers with a measuring force control), this will lead to a reduced uncertainty (Table 2.). There is only one dominating rectangular contribution in this budget. Therefore, expanded uncertainty in this case will be:

$$U = k \cdot u(E_X) = 0.95\sqrt{3} \cdot 0.15 = 0.0247\,\text{mm}.$$

The coverage factor $0.95\sqrt{3}$ for rectangular distribution was taken from the formula (S9.8) [9].

It should be noted that even in this case the condition *U*<*MPE*/3, given in [3], is not observed.

Table 2. Uncertainty budget of calibration of Vernier caliper with measuring force control.

quantity X_i	estimate x_i	standard uncertainty $u(x_i)$	probability distribution	sensitivity coefficient c_i	uncertainty contribution $u_i(y)$
l_{iX}	150.10 mm	–	–	–	–
l_S	150.00 mm	0.46 μm	rectangular	-1.0	- 0.46 μm
Δt	0	1.15 K	rectangular	1.7 μmK^{-1}	2.0 μm
δl_{iX}	0	14.4 μm	rectangular	1.0	14.4 μm
δl_M	0	3.3 μm	triangular	1.0	3.3 μm
E_X	0.10 mm	–	–	–	15 μm

It should be noted that the expression (1) is true for probability compliance of no more than 0.95. In general, in the documents [7]-[8] it is proposed to evaluate the probability of compliance of IMIs in the following way:

$$p_c = \Phi_N\left(\frac{USL - |y|}{u}\right) = \Phi_N\left(\frac{\text{MPE} - |\widehat{E}_X|}{u}\right) = \Phi_N(z), \quad (2)$$

where $\Phi_N(z)$ – standard normal distribution function with variable z, $\widehat{E}_X$, u – estimation of IMI's indication error and its standard uncertainty, respectively.

To find $\Phi_N(z)$, it is proposed [8] to use the standard normal distribution table (p. 53). However, when calibrating a large number of IMIs, such as Vernier calipers, the distribution function attributed measurand is often trapezoidal or even rectangular. This is due to the fact that the dominant sources of uncertainty of the calibrated IMI are often rectangular distributed corrections, such as the correction of the Vernier caliper resolution [9].

The cumulative distribution function (CDF) of the trapezoidal distribution, which is a convolution of two uniform distributions with the ratio of standard uncertainties $\gamma = u_2/u_1 \le 1$, has the form:

$$F_T(z) = \begin{cases} 0, & z < -\text{A}; \\ \dfrac{[z\sqrt{1+\gamma^2} + \sqrt{3}(1+\gamma)]^2}{24\gamma}, & -\text{A} \le z < -\text{B}; \\ \dfrac{z\sqrt{1+\gamma^2} + \sqrt{3}}{2\sqrt{3}}, & -\text{B} \le z < \text{B}; \\ 1 - \dfrac{[\sqrt{3}(1+\gamma) - z\sqrt{1+\gamma^2}+]^2}{24\gamma}, & \text{B} \le z < \text{A}; \\ 1, & z \ge \text{A}. \end{cases} \quad (3)$$

where $A = \sqrt{3}(1+\gamma)/\sqrt{1+\gamma^2}$; $B = \sqrt{3}(1-\gamma)/\sqrt{1+\gamma^2}$.

For trapezoidal distribution with γ =0.5 (Table 1.) and considering $z = (MPE - |\widehat{E}_X|)/u$, we have:

at $|\widehat{E}_X|$ =0, $z = \dfrac{0.05}{0.0325} = 1.538$, that is $p_c = 0.936 < 0.95$;

at $|\widehat{E}_X|$ =0.025, $z = \dfrac{0.025}{0.0325} = 0.769$, that is $p_c = 0.75$;

at $|\widehat{E}_X|$ =0.05, $z = 0$, therefore $p_c = 0.5$.

The rectangular CDF has the form:

$$F_R(z) = \begin{cases} 0, & z < -\sqrt{3}; \\ (z+\sqrt{3})/2\sqrt{3}, & z \in [-\sqrt{3}; \sqrt{3}]; \\ 1, & z > \sqrt{3}. \end{cases} \quad (4)$$

For the rectangular distribution and data of Table 2., we have:

at $|\widehat{E}_X|$ =0, $z = \dfrac{0.05}{0.015} = 3.33 > \sqrt{3}$, that is $p_c = 1$,

at $|\widehat{E}_X|$ =0.025, $z = \dfrac{0.025}{0.015} = 1.67 < \sqrt{3}$, that is $p_c = 0.98$,

at $|\widehat{E}_X|$ =0.05, $z = 0$, therefore $p_c = 0.5$.

Thus, a caliper will be usable with a probability of more than 0.95 if its readings do not deviate from the value of the end length gauge or equal to 0.5 MPE. Practice shows that the number of such calipers is about 60 % of those arrived at the test. Thus, 40 % of the verified Vernier calipers are unusable.

Fig.1. shows the CDF for the uniform, triangular, trapezoidal, and normal distribution laws.

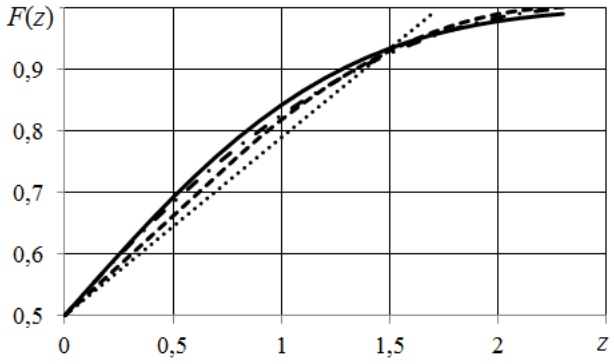

Fig.1. CDF $F(z)$ for uniform (···), trapezoidal (---) with γ = 0.5, triangular (–•–), and normal (—) distribution laws.

From Fig.1. it is seen that the CDF for the triangular and normal laws practically coincide (with an error of no more than 2 % in probability), therefore, instead of a table with values of the normalized normal distribution given in [8], one can use the dependence for the triangular distribution law:

$$F_T(z) = \begin{cases} 0, & z < -\sqrt{6}; \\ (z+\sqrt{6})^2/12, & -\sqrt{6} \le z < 0; \\ 1-(\sqrt{6}-z)^2/12, & 0 \le z < \sqrt{6}; \\ 1, & z \ge \sqrt{6}. \end{cases} \quad (5)$$

The formulas (2) - (4) are obtained for rectangular, triangular and trapezoidal distributions of variable with zero expectations and unit standard deviations. However, these models are only an approximation of the real law of distribution obtained as a result of calibrations. In those cases, we recommend to evaluate the probability of compliance with help of the Monte Carlo method [10].

2.2. Monte Carlo procedure

Monte Carlo procedure for construction of distribution function includes the following operations, registered in uncertainty budget (Table 3.):

Table 3. Uncertainty budget.

input quantity	estimate	standard uncertainty	probability distribution	sensitivity coefficient	uncertainty contribution
X_1	x_1	$u(x_1)$	PDF 1	c_1	$u_1(\widehat{E}_X)$
X_2	x_2	$u(x_2)$	PDF 2	c_2	$u_2(\widehat{E}_X)$
:	:	:	:	:	:
X_N	x_N	$u(x_N)$	PDF N	c_N	$u_N(\widehat{E}_X)$
output quantity	estimate	combined standard uncertainty	coverage probability	coverage factor	expanded uncertainty
E_X	$\widehat{E}_X$	$u_c(\widehat{E}_X)$	0.95	k	U

1. Recording the model equation:

$$E_X = f(X_1, X_2, ..., X_N), \quad (6)$$

where $X_1, X_2, ..., X_N$ - input quantities (first column of the Table 3.).

2. Evaluation of the input quantities as $x_1, x_2, ..., x_N$ (second column of the Table 3.).

3. Evaluation of standard uncertainties of the input quantities as $u(x_1), u(x_2), ..., u(x_N)$ (third column of the Table 3.).

4. Assigning the probability density functions (PDFs) for input quantities (fourth column of the Table 3.).

5. Selecting the number M of Monte Carlo trials to be made ($M \ge 10^4$).

6. Generating M trials of measurand for vector, by sampling from the assigned PDFs as realizations of the (set of N) of the input quantities X_i .

7. For each such vector, forming the corresponding model value of E_X , yielding M model values E_{Xi} .

8. Calculation of an estimate $\bar{E}_X$ of E_X by the formula:

$$\bar{E}_X = \frac{1}{M}\sum_{i=1}^{M} E_{X\,i}\,. \tag{7}$$

9. Calculation of unbiased estimate E^*_{Xi} using the formula:

$$E^*_{Xi} = E_{Xi} - \bar{E}_X\,. \tag{8}$$

10. Sorting these M model values E^*_{Xi} into strictly increasing order, using the sorted model values to provide an implementation of the propagation of distributions G [10].

11. Calculating the values of probability

$$p(i) = 100 \cdot i/M\,,\ i = 1 \ldots M,$$

which correspond to the values of E^*_{Xi}.

12. Construction of dependence $p(i) = E^*_{Xi}$.

13. Finding the probability of compliance p_c for the value of

$$E^*_{Xi} = MPE - \left|\bar{E}_X\right|.$$

Realization of the steps 6-8 of the above described Monte Carlo procedure gives the dependence $p_c(\mathrm{MPE} - |E_X|)$, represented in Fig.2.

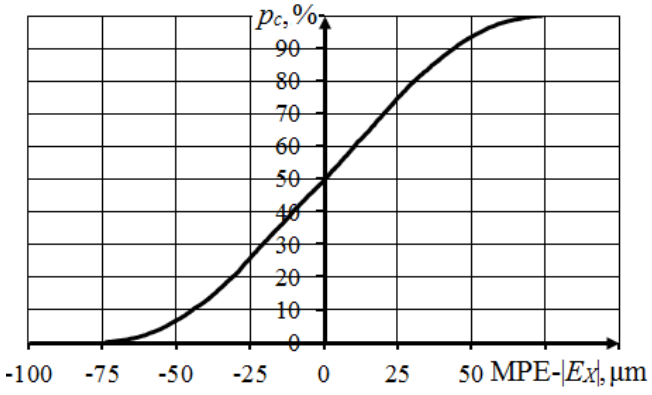

Fig.2. Dependence p_c of $\mathrm{MPE} - |E_X|$.

3. Conclusions

The approaches for compliance probability determination of the IMIs with the specification requirements taking into account the uncertainty of the measurements for the abnormal laws of distribution of their error are presented.

The examples adduced in the article show that for all distribution laws the condition *U <MPE/3* given in [3] is not observed.

When carrying out verification of the IMIs applied in the legal metrology, it would also be necessary to take into account the uncertainty of measurements.

References

[1] International Organization for Standardization. (2005). *General requirements for the competence of testing and calibration laboratories*. ISO/IEC 17025:2005.

[2] EURACHEM/CITAC Working Group. (2012). *Quantifying Uncertainty in Analytical Measurement. EURACHEM / CITAC Guide CG4, Third Edition*. ISBN 978-0-948926-30-3.

[3] International Organization for Standardization. (2003). *Statistical methods – Guidelines for the evaluation of conformity with specified requirements – Part 1: General principles*. ISO 10576-1:2003.

[4] EURACHEM/CITAC Working Group. (2007). *Use of uncertainty information in compliance assessment. EURACHEM / CITAC Guide, First Edition.*

[5] International Organization for Standardization. (2013). *Geometrical product specifications (GPS) – Inspection by measurement of workpieces and measuring equipment – Part 1: Decision rules for proving conformity or nonconformity with specifications.* ISO 14253-1:2013.

[6] Eurolab. (2008). *Determination of conformance with specifications or limit values with particular reference to measurement uncertainties – possible strategies.* EUROLAB "Cook Book" – Doc No. 8.0. www.eurolab.org/documents/Cookbook_No_8.pdf.

[7] Joint Committee for Guides in Metrology. (2012). *Evaluation of measurement data – The role of measurement uncertainty in conformity assessment.* JCGM 106:2012.

[8] International Organization of Legal Metrology. (2017). *The role of measurement uncertainty in conformity assessment decisions in legal metrology*. OIML G 19, Edition 2017 (E).

[9] EA Laboratory Committee. (2013). *Evaluation of the Uncertainty of Measurement In Calibration.* EA-4/02 M: 2013.

[10] Joint Committee for Guides in Metrology. (2008). *Evaluation of measurement data – Supplement 1 to the "Guide to the expression of uncertainty in measurement" – Propagation of distributions using a Monte Carlo method.* JCGM 101:2008.

[11] International Organization for Standardization. (2003). *Statistical methods – Guidelines for the evaluation of conformity with specified requirements – Part 1: General principles*. ISO 10576-1:2003.

Received September 9, 2017.
Accepted November 13, 2017.

MEASUREMENT SCIENCE REVIEW, **17**, (2017), No. 6, 273-281

DE GRUYTER OPEN

MEASUREMENT SCIENCE REVIEW

Journal homepage: http://www.degruyter.com/view/j/msr

ISSN 1335-8871

The Enhancement of 3D Scans Depth Resolution Obtained by Confocal Scanning of Porous Materials

Dalibor Martisek, Jana Prochazkova

Institute of Materials Science and Engineering, NETME center, Brno University of Technology, Czech Republic, martisek@fme.vutbr.cz, prochazkova.j@fme.vutbr.cz

The 3D reconstruction of simple structured materials using a confocal microscope is widely used in many different areas including civil engineering. Nonetheless, scans of porous materials such as concrete or cement paste are highly problematic. The well-known problem of these scans is low depth resolution in comparison to the horizontal and vertical resolution. The degradation of the image depth resolution is caused by systematic errors and especially by different random events. Our method is focused on the elimination of such random events, mainly the additive noise. We use an averaging method based on the Lindeberg–Lévy theorem that improves the final depth resolution to a level comparable with horizontal and vertical resolution. Moreover, using the least square method, we also precisely determine the limit value of a depth resolution. Therefore, we can continuously evaluate the difference between current resolution and the optimal one. This substantially simplifies the scanning process because the operator can easily determine the required number of scans.

Keywords: Noise reduction, porous materials, confocal microscope, 3D scans, 3D reconstruction.

1. INTRODUCTION

The 3D reconstruction based on laser scanning confocal microscopy is an indispensable tool for civil engineering. Particularly in civil engineering, many different porous materials must be analysed. Common examples include the micro fractures in the concrete or the cement paste. However, the depth resolution of these scans is substantially influenced by additive noise and other disturbing factors. The described work is a result of cooperation between the Faculty of Civil Engineering and the Faculty of Mechanical Engineering, BUT that is focused on the precise evaluation of the concrete material properties.

In this article, we propose a method that eliminates the vast majority of the additive noise without degradation of useful information. This allows enhancing the depth resolution of the scans to the order comparable with horizontal and vertical resolution. Firstly, we describe the mathematical apparatus of our method. Subsequently, we assess our method with statistical evaluation and compare our results with methods used in common software tools that are provided with the microscopes.

2. SUBJECT & METHODS

2.1. Material and current methods

Our method follows on the recently published work on morphological analysis of fracture surfaces [2], [3] and also, porous materials in [1]. The gist of our work is the improvement of *z*-resolution that determines the quality of the reconstruction. The overview of common approaches used for 3D reconstruction can be found in [6], [9].

The *z*-resolution, i.e. optical sectioning thickness, depends on many factors: the wavelength of the used light, pinhole size, numerical aperture of the objective lens, refractive index of components in the light path, and the assembly of the instrument. The degradation of the *z*-resolution is often caused by systematic errors and by random events. Systematic errors, for example imperfections of the lens, light diffraction, are not random so that they cannot be detected and eliminated by existing methods that work only with random events. For example, the authors [5] use the weighted window function to reduce the Poisson noise in confocal scanning. Also, our previous article [7] describes the methods to eliminate noise. But the systematic errors are not random so these methods are not able to eliminate it.

Especially, additive noise is added to original values during the making, transfer or reproduction of an image.

In our work, we deal with the random events reduction, especially additive noise, to improve *z*-resolution.

During measurement, we scan the same point of the sample twice with the same conditions. In the case of noiseless measurements, we would get two identical results. Nevertheless, different values indicate the presence of noise. From the mathematical point of view, we consider everything what causes this difference as the noise (typically heat vibrations, also measurement errors, mechanical oscillations, etc.)

DOI: 10.1515/msr-2017-0034

Let us mention some methods for reducing additive noise – Richardson-Lusy algorithm (*RLA*), Maximum Likelihood Estimation (*MLE*), and Iterative Constrained Tikhonov-Miller (*ICTM*) algorithm [4]. However, these methods are limited by the additional assumptions, e.g. Poisson distribution of noise [5]. Low-pass filters are commonly used to reduce the additive noise as well [9]. The key purpose of these filters is the reduction of high spatial frequencies in the signal in the sense of the Fourier transform. Nevertheless, these filters are not able to differentiate whether the high-frequency information is caused by noise or by high contrast in the image. Therefore, loss of information necessarily ensues.

Our recent work [7] presents the method based on the Lindeberg-Lévy theorem as the pre-processing tool for single 2D images. In this paper, we introduce the application of this approach in confocal scanning to eliminate the random events (additive noise) and improve the *z*-resolution to the same values as the *xy*-resolution. We perform a statistical comparison of our results with the standard commercial software solution (Olympus software, version 6). The results are summarised in Section 3 and in Appendix, Table 4. and Table 5.

Table 4. shows that the average of seven or eight following measurements gives the results comparable with a low-pass filtered surface. The accuracy is higher with the increasing number of measurements and the correlation reaches the approximate value 0.999872 for K=25.

All sample measurements were made with confocal microscope Olympus LEXT OLS 3100. This microscope includes a confocal mode which collects the data to the Comma Separated Values (CSV) file with step 0.62 μm in the *z*-axis. This value may lead to the conviction that the measured surface has the same accuracy. Nevertheless, this confidence is quite false in the case of porous materials as is shown in Section 3. We use the confocal mode with the field of vision 2560× 1920 μm at a pixel resolution of 1024×768 pixels. It follows that the xy-resolution was 2.5 μm.

We work with the sample of fracture surface of hydrated Portland cement paste. For illustrative purposes, several specimens consisting of hydrated cement pastes were selected from a set of one-year old specimens. Ordinary Portland cement was used for their preparation. The specimens were mixed with the water-to-cement ratio equal to 0.4, and the fresh paste was cast in moulds of the size 2x2x10 cm^3. The paste was cured at a temperature of 20±2°C, and relative humidity of 100 % for three months. The specimens were then fractured in the three-point bending arrangement and sectioned into small cubes 2x2x2 cm^3. The rest of the time the cubes were stored under normal laboratory conditions (20±2 C, 101 325 kPa, 60±10 % RH).

2.2. Statistical evaluation

This section describes the statistical evaluation that is used in other sections to evaluate the results. We use these parameters: root mean square error, (relative) average difference, and Pearson's correlation coefficient.

Denote P, Q results of two different scans of the same profile, P_{ij}, Q_{ij} values of pixel $[i, j]$ in profiles P, Q, W, and H width and height of profile matrices of P, Q. Then the root mean square error is defined as:

$$RMSE = \sqrt{\frac{1}{W \cdot H}\sum_{i=1}^{W}\sum_{j=1}^{H}\left(P_{ij} - Q_{ij}\right)^2}$$

The average difference:

$$AD = \frac{1}{W \cdot H}\sum_{i=1}^{W}\sum_{j=1}^{H}\left|P_{ij} - Q_{ij}\right|$$

the relative average difference:

$$RAD = \frac{AD}{\Delta z} = \frac{1}{\Delta z}\cdot\frac{1}{W \cdot H}\sum_{i=1}^{W}\sum_{j=1}^{H}\left|P_{ij} - Q_{ij}\right|$$

where $\Delta z = 0.62\ \mu m$ is the used step in the z-axis. The value RAD indicates how many times the real accuracy is less than the step in the z-axis. Finally, Pearson's correlation coefficient

$$CORR = \frac{\sum_{i=1}^{W}\sum_{j=1}^{H}\left(P_{ij} - \bar{P}\right)\left(Q_{ij} - \bar{Q}\right)}{\sqrt{\sum_{i=1}^{W}\sum_{j=1}^{H}\left(P_{ij} - \bar{P}\right)^2 \sum_{i=1}^{W}\sum_{j=1}^{H}\left(Q_{ij} - \bar{Q}\right)^2}}$$

where $\bar{P},\ \bar{Q}$ are arithmetic means of profiles $P;\ Q$.

2.3. Noise decreasing method

Proposed noise reduction method is based on the Lindeberg-Lévy Central Limit Theorem, which produces more accurate results in comparison with low-pass filters and can be used without any limitations, unlike *RLA*, *MLE* or *ICTM*.

Consider the noise as the realization of a random variable. Then we can say:

Theorem (Lindeberg-Lévy Central Limit Theorem). *Let $X_1; X_2; \ldots; X_K$ be random variables with arbitrary (but the same) distribution, the same mean value μ and the same (finite) variance σ^2. Then the mean of $X_1; X_2; \ldots; X_K$ for $K \to \infty$ converges to the normal distribution with the same mean value μ and variance $\acute{\sigma}^2 = \sigma^2/K$.*

The proof of this theorem can be found in [8] for example. Generally, the application of the theorem causes that the mean variance of K random variables is K-times lower. This will be described further.

Let P be the input profile that consists of the useful information U and the noise N. The noise N is the realization of a random variable with expected values equal to zero. We carry out the profile measurements K-times, therefore we obtain the series $\{P(k)\}$, $k = 1, 2, \ldots, K$. Let U_{ij} be the useful information and $N_{ij}(k)$ be the random noise in pixel $[i, j]$ in

profile $P(k)$. The arithmetic means in $[i,j]$-th pixel can be expressed as:

$$\overline{P_{ij}(K)} = \frac{1}{K}\cdot\sum_{k=1}^{K} P_{ij}(k) = \frac{1}{K}\cdot\sum_{k=1}^{K}\left(U_{ij} + N_{ij}(k)\right) = U_{ij} + \frac{1}{K}\cdot\sum_{k=1}^{K} N_{ij}(k) \tag{1}$$

The useful information U_{ij} (it is not random) is preserved and noise is:

$$N_{ij} = \frac{1}{K}\cdot\sum_{k=1}^{K} N_{ij}(k) \tag{2}$$

Equation (2) denotes that the mean is equal to zero and the variance is K-times lower.

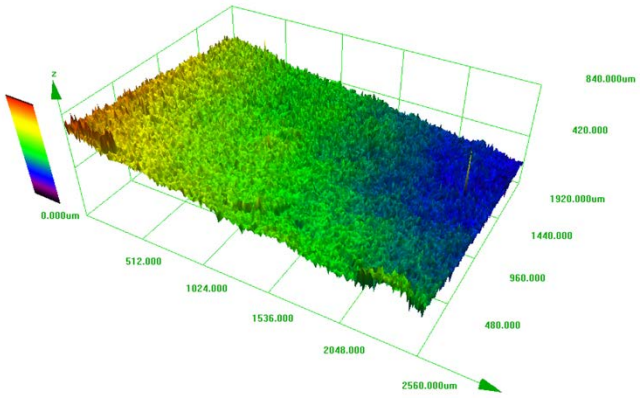

Fig.1. Non-filtered profile reconstructed with Olympus company software (step 0.62 μm in the z-axis) technology.

We use different statistical variables to compare our results. Let $\overline{P_{ij}(K)}$ be the arithmetic mean of K values in pixel $[i,j]$ in K scannings of the same profile. Let $\overline{Q_{ij}(K)}$ be the arithmetic mean of the following K values in pixel $[i,j]$ in the following K scannings of the same profile. Denote $RMSE(K)$, $AD(K)$; $RAD(K)$; $CORR(K)$ the root mean square error, average difference, relative average difference, and correlation of $\overline{P_{ij}(K)}$ and $\overline{Q_{ij}(K)}$, i.e.

$$RMSE(K) = \sqrt{\frac{1}{W\cdot H}\sum_{i=1}^{W}\sum_{j=1}^{H}\left(\overline{P_{ij}(K)} - \overline{Q_{ij}(K)}\right)^2}$$

where

$$\overline{P_{ij}(K)} = U_{ij}(K) + \frac{1}{K}\cdot\sum_{k=1}^{K} N_{ij}^{(P)}(k)$$

$$\overline{Q_{ij}(K)} = U_{ij}(K) + \frac{1}{K}\cdot\sum_{k=1}^{K} N_{ij}^{(Q)}(k)$$

It means

$$RMSE(K) = \frac{1}{K}\cdot\sqrt{\frac{1}{W\cdot H}\sum_{i=1}^{W}\sum_{j=1}^{H}\left(\sum_{k=1}^{K} N_{ij}^{(P)}(k) - \sum_{k=1}^{K} N_{ij}^{(Q)}(k)\right)^2} = \frac{1}{K}\cdot\sqrt{\frac{1}{W\cdot H}\sum_{i=1}^{W}\sum_{j=1}^{H}\left(\sum_{k=1}^{K}\left[N_{ij}^{(P)}(k) - N_{ij}^{(Q)}(k)\right]\right)^2} = \frac{1}{K}\cdot\sqrt{\frac{1}{W\cdot H}\sum_{i=1}^{W}\sum_{j=1}^{H}\left(\sum_{k=1}^{K} N_{ij}(k)\right)^2} \tag{3}$$

Similarly,

$$AD(K) = \frac{1}{K}\cdot\left[\frac{1}{W\cdot H}\sum_{i=1}^{W}\sum_{j=1}^{H}\left|\sum_{k=1}^{K} N_{ij}(k)\right|\right] \tag{4}$$

The expression $\sum_{k=1}^{K} N_{ij}(k)$ in (1), (2) describes the noise. Therefore, the expressions under the square root in (3) or whole expression in the square brackets (4) also determine the noise. This means that $RMSE(K)$ and $AD(K)$ are proportional to K inversely (where K denote the number of averaged scans).

Analogically, we can write:

$$RAD(K) = \frac{AD}{\Delta z} = \frac{1}{K}\cdot\frac{1}{\Delta z}\cdot\frac{1}{W\cdot H}\sum_{i=1}^{W}\sum_{j=1}^{H}\left|P_{ij}(K) - Q_{ij}(K)\right|$$

Correlation can be expressed as:

$$CORR(K) = \frac{\sum_{i=1}^{W}\sum_{j=1}^{H}\left(P_{ij}(K) - \overline{P(K)}\right)\left(Q_{ij}(K) - \overline{Q(K)}\right)}{\sqrt{\sum_{i=1}^{W}\sum_{j=1}^{H}\left(P_{ij}(K) - \overline{P(K)}\right)^2\sum_{i=1}^{W}\sum_{j=1}^{H}\left(Q_{ij}(K) - \overline{Q(K)}\right)^2}}$$

Note, that $0 < CORR,\ CORR < CORR(K), CORR(K) < 1$ and we can write $0 < CORR < CORR(K) < 1$.

3. Results and Discussion

As mentioned above, the Olympus LEXT OLS 3100 confocal microscope was used to acquire a CSV data file that describes the fracture surface of hydrated Portland cement paste (step 0.62 µm in the z-axis). For illustration, we show the surface reconstruction using Olympus company software in Fig.1. It confirms that reconstruction of porous materials is problematic and obviously, the image is also constructed with low resolution.

Fig.2. clearly shows that the reconstructed surface (by Olympus software) also contains a huge error. This error is clearly visible in Table 3. in Appendix where we compare the image section of two subsequent scans of the same area.

The differences covered the interval $-262\,\mu m$ to $+114\,\mu m$. Note that the z-step is $0.62\,\mu m$. For comparison,

we make the reconstruction of the same data using our proposed visualization software Micro3D.

We make five pairs $P^{(k)}; Q^{(k)}; \ k = 1,2,\dots,5$ of same sample measurements. We compute the statistical characteristics $RMSE^{(k)}; \ AD^{(k)}; \ RAD^{(k)} \ CORR^{(k)}; \ k = 1,2,\dots,5$ for each pair of these measurements. For each k, $P^{(k)}$ and $Q^{(k)}$ are measurements of the same profile, i.e. for each $k = 1,2,\dots,5$ the ideal values are: $RMSE^{(k)} = 0;$ $AD^{(k)} = 0; RAD^{(k)} = 0\ \%; CORR^{(k)} = 100\ \%$. As we can see from Table 1., the average difference AD is approximately $23.5\ \mu m$, the measurement error is therefore approximately 38 times higher than the used step $0.62\ \mu m$. The correlation reaches the value 97 %.

Moreover, we filtered this data using Olympus company low-pass filter, and Table 2. presents the same characteristics as Table 1. The values of statistical parameters are significantly better. However, these filters are not able to differentiate whether the high-frequency information is a useful signal or the noise.

Therefore, low-pass filters decrease additive noise but also degrade the reconstructed surface. We can see this fact on the visualization. The surface reconstructed by Olympus Company software is presented in Fig.3. It is evident that low-pass filters are not suitable for porous materials because of the visible surface degradation.

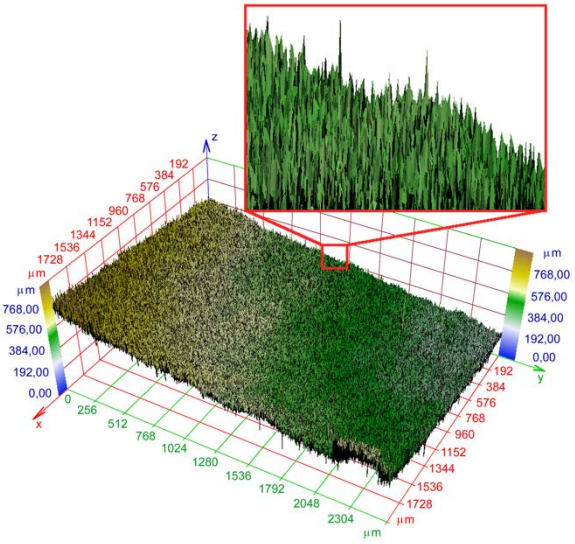

Fig.2. Non-filtered profile reconstructed with Micro3D software (same data as in Fig.1.)

Table 1. Comparison of five pairs of the same surface scans, non-filtered. (z-step 0.62 μm).

k	RMSE	AD	RAD	CORR
1	29.9229	23.4072	37.75	0.971787
2	29.944	23.4163	37.77	0.971762
3	29.9208	23.3903	37.73	0.971791
4	29.9884	23.4303	37.79	0.971667
5	30.0563	23.5059	37.91	0.971549

Table 2. The comparison of five pairs of the same surface scans filtered using Olympus company low-pass filter. (z-step 0.62 μm).

k	RMSE	AD	RAD	CORR
1	6.0940	4.5698	7.37	0.998676
2	6.1739	4.1664	6.72	0.998642
3	6.2504	4.6749	7.54	0.998610
4	6.3048	4.7052	7.59	0.998585
5	6.4391	4.7829	7.71	0.998529

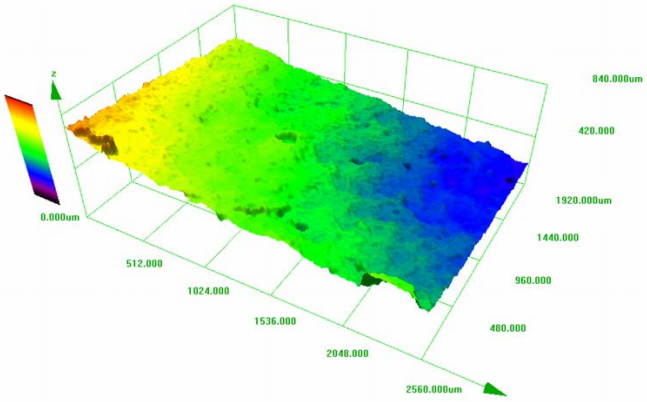

Fig.3. Profile from Fig.1. filtered by a common low-pass filter (Olympus company software).

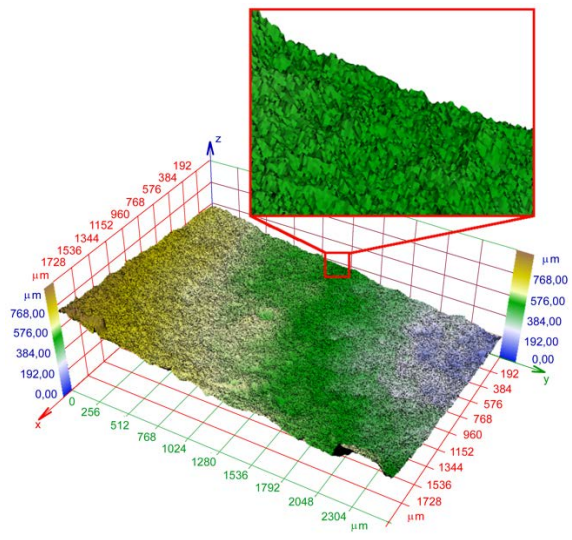

Fig.4. The surface composed of average values given by 25 scans - sample S_1 (Micro3D software).

The following part presents the advantage of the proposed noise reduction method using different statistical evaluation.

We make sequence of 25 pairs $P^{(k)}; Q^{(k)}; k = 1,2,\dots,25$ of the sample S_1 measurements. Consequently, we calculated 25 pairs of averages of K profiles.

$$\overline{P(K)} = \frac{1}{K}\sum_{k=1}^{K} P^{(k)}; \qquad \overline{Q(K)} = \frac{1}{K}\sum_{k=1}^{K} Q^{(k)}; \qquad K = 1, 2, \ldots, 25 \tag{5}$$

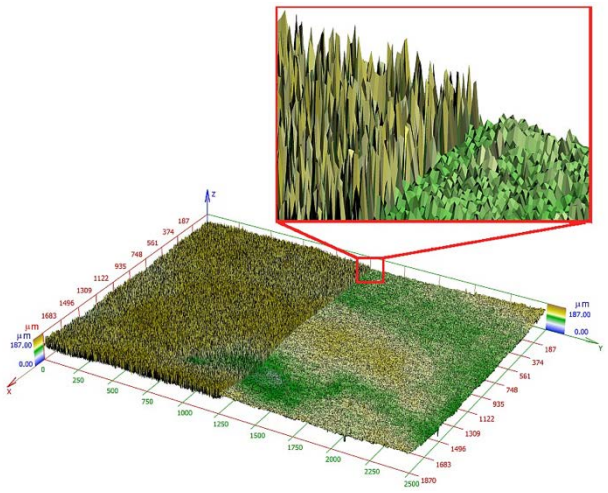

Fig.5. The surface composed of average values given by 25 scans - sample S_2 (Micro3D software).

For example, $\overline{P(10)}$ is the profile matrix calculated as the arithmetic mean of ten measurements $P^{(1)}$; $P^{(2)}$,..., $P^{(10)}$ of the same profile and $\overline{Q(10)}$ is the profile matrix calculated as the arithmetic mean of other ten measurements $Q^{(1)}$, $Q^{(2)}$,...;, $Q^{(10)}$ of the same profile. We compute the statistical characteristics between $\overline{P(K)}$ and $\overline{Q(K)}$ in dependence on the value of *K*.

Due to the Lindeberg-Lévy Central Limit Theorem, we eliminate the noise using (1), (2). Following computation of the statistical characteristics $RMSE(K)$, $AD(K)$, $RAD(K)$, and $CORR(K)$ between $\overline{P(K)}$ and $\overline{Q(K)}$ proves that the method improves the *z*-resolution significantly. The results in Table 4. show that the average of seven or eight following measurements *(K=7, 8)* gives the results comparable with a low-pass filtered surface. The accuracy is higher with the increasing number of measurements. The correlation reaches the approximate value 0.999872 for *K=25*. The surface composed of average values given by 25 scans is presented in Fig.4.

We make the measurement and the same computations as described in previous part for the second sample S_2 (profile of hydrated Portland cement paste). The analogy data to Table 4. are in Table 5., and the resulting surface is in Fig.5. (analogical to Fig.4.).

Due to the inverse proportion of $RMSE(K)$ and $AD(K)$ predicted in Section 2., measured data was fitted with a function $f(K) = \frac{a}{K} + b$ by the least squares method.

We obtain for the first sample data these equations:

$$RMSE(K) = \frac{a}{K} + b \approx \frac{27{,}32}{K} + 2.63 \tag{6}$$

$$AD(K) = \frac{c}{K} + d \approx \frac{22{,}15}{K} + 1.82 \tag{7}$$

The functions (6) and (7) are drawn in Fig.6. The noise variance gives the numerators in these equations. The additive constant *d* in (7) describes the difference from a supposed inverse proportion. This difference is probably caused by some non-random measurement error of the microscope. The additive constant depicts that even in the case of perfect additive noise reduction ($K \to \infty$) it is not possible to reconstruct the profile exactly. The limit precision is $\pm\frac{d}{2} \approx \pm 0{,}9\ \mu m$.

The sample S_2 values of a, b, c, d in (6), (7) are equal to $a = 27.04$; $b = 2.78$; $c = 21.92$; $d = 2.06$ and corresponding functions are in Fig.7.

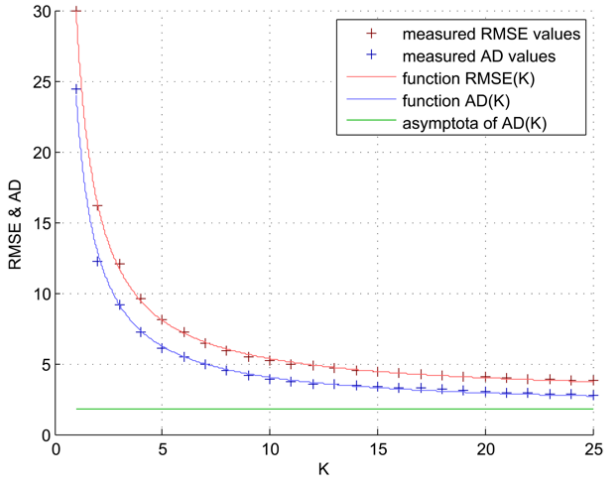

Fig.6. Functions *RMSE* and *AD* for sample S_1 – reliance of Root Mean Square Error and Average Difference on the number of averaged scans.

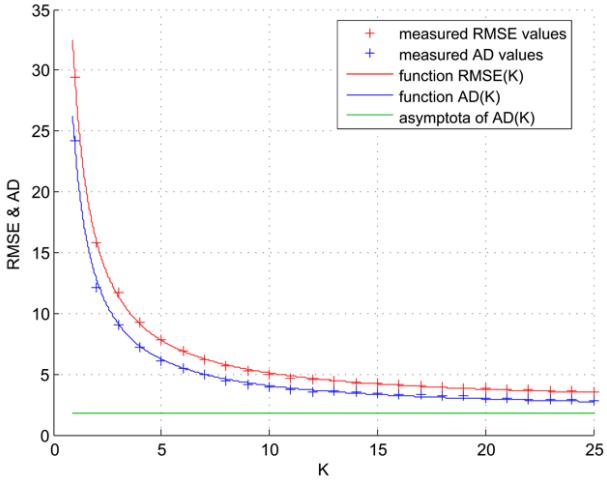

Fig.7. Functions *RMSE* and *AD* for sample S_1 – reliance of Root Mean Square Error and Average Difference on the number of averaged scans.

4. CONCLUSIONS

We have used the field of vision 2560× 1920 μm, a pixel resolution of 1024×768 pixels so that the xy-resolution was 2.5 μm. In our case, the z-resolution of input data was 0.62 μm. The course of the function $AD(K)$ indicates that we can improve the resolution even with low-quality data using 4-6 subsequent scans. The usage of 25 scans causes the improvement of z-axis resolution on the level comparable to the xy-resolution. Theoretically, due to additive constant d, maximal additive noise reduction ($K \to \infty$) means that the maximal resolution for tested samples is $\pm\frac{d}{2} \approx \pm 0.9\ \mu m$, and $\pm\frac{d}{2} \approx \pm 1.0\ \mu m$, i.e. three and 2.5 times higher resolution in comparison with xy-resolution. This method based on the Lindeberg–Lévy theorem is able to set the optimal number of measurements to get the required depth precision.

ACKNOWLEDGMENT

The authors acknowledge support from Project LO1202 by financial means from the Ministry of Education, Youth and Sports, the National Sustainability Programme I. The authors thank prof. Tomas Ficker from the Faculty of Civil Engineering of Brno University of Technology for the provided data.

REFERENCES

[1] Ficker, T., Len, A., Chmelík, R., Lovicar, L., Martišek, D., Němec, P. (2007). Fracture surfaces of porous materials. *Europhysics Letters*, 80 (6), 1600-1604.

[2] Ficker, T., Martišek, D., Jennings, H.M. (2010). Roughness of fracture surfaces and compressive strength of hydrated cement pastes. *Cement and Concrete Research*, 40 (6), 947-955.

[3] Ficker, T., Martišek, D. (2012). Digital fracture surfaces and their roughness analysis: Applications to cement-based materials. *Cement and Concrete Research*, 42 (6), 827-833.

[4] Van Kempen, G.M.P., Van Vliet, L.J., Verveer, P.J., Van Der Voort, H.T.M. (1997). A quantitative comparison of image restoration methods for confocal microscopy. *Journal of Microscopy*, 185, 354-365.

[5] Kervrann, C., Trubuil, A. (2004). An adaptive window approach for Poisson noise reduction and structure preserving in confocal microscopy. In *2nd IEEE International Symposium on Biomedical Imaging: Nano to Macro*, Arlington, VA, USA. IEEE, 788-791.

[6] Sheppard C.J.R., Shotton D.M. (1997) *Confocal Laser Scanning Microscopy*. Springer.

[7] Martisek, D., Prochazkova, J., Ficker, T. (2015). High-quality three-dimensional reconstruction and noise reduction of multifocal images from oversized samples. *Journal of Electronic Engineering*, 24 (5).

[8] Montgomery, D.C., Runger, G.C. (2003). *Applied Statistics and Probability for Engineers*, 3rd ed. John Wiley & Sons.

[9] Yio, M.H.N., Mac, M.J., Wong, H.S., Buenfeld, N.R. (2015). 3D imaging of cement-based materials at submicron resolution by combining laser scanning confocal microscopy with serial sectioning. *Journal of Microscopy*, 258 (2), 151-169.

Received May 19, 2017.
Accepted November 13, 2017.

APPENDIX

Table 3. Two submatrices of heights of the same sample points acquired by two subsequent scans (z-step 0.62 μm) and their differences (all in micrometers).

First scanning

542.85	562.70	556.07	566.79	553.22	545.08	274.90	554.55	576.03	506.31	518.87	523.18	556.51
538.57	568.27	560.31	576.65	509.64	516.04	526.16	550.84	543.13	596.15	539.87	570.22	588.08
588.11	570.42	559.23	558.35	572.98	563.72	541.97	571.48	550.09	492.95	551.80	555.34	571.24
560.49	577.91	599.61	573.03	586.78	564.28	563.84	587.45	554.41	577.02	577.18	559.52	554.95
563.75	559.75	624.12	573.59	552.75	521.04	531.06	601.79	574.48	571.30	560.83	560.34	585.82
552.68	540.69	547.04	563.95	552.87	558.38	568.50	549.32	539.15	559.13	559.33	557.79	536.69
567.29	580.02	569.31	569.65	553.17	538.72	489.03	519.95	544.29	570.86	573.38	554.37	569.80

Second scanning

580.01	531.17	580.64	529.34	545.78	539.43	536.89	603.34	537.14	554.97	548.45	565.95	555.79
555.20	557.44	556.71	574.78	559.01	571.09	564.41	560.34	582.43	572.75	507.05	538.50	544.71
519.34	548.63	552.61	559.06	567.07	584.37	559.08	557.77	554.29	569.76	538.78	557.55	542.16
531.10	577.58	529.96	550.27	575.13	568.18	552.65	533.79	537.70	548.60	566.12	488.60	508.98
568.32	558.87	510.08	563.84	566.87	573.43	564.06	517.01	514.14	586.94	542.68	515.10	529.12
545.59	570.74	582.44	581.88	559.33	537.92	565.95	564.70	557.55	580.76	555.95	487.07	561.33
576.52	564.66	545.22	581.80	525.63	576.65	577.54	563.64	546.92	541.52	529.59	568.95	581.74

Differences

-37.16	31.53	-24.57	37.45	7.45	5.64	**-261.98**	-48.79	38.89	-48.66	-29.58	-42.77	0.73
-16.63	10.84	3.60	1.86	-49.36	-55.05	-38.25	-9.49	-39.30	23.39	32.82	31.72	43.37
68.77	21.78	6.62	-0.71	5.91	-20.65	-17.11	13.71	-4.20	-76.80	13.02	-2.21	29.08
29.39	0.32	69.65	22.76	11.65	-3.89	11.19	53.66	16.72	28.42	11.06	70.92	45.96
-4.56	0.88	**114.04**	9.76	-14.13	-52.39	-33.00	84.78	60.34	-15.64	18.14	45.23	56.70
7.08	-30.04	-35.41	-17.93	-6.45	20.45	2.55	-15.39	-18.40	-21.63	3.37	70.71	-24.64
-9.23	15.36	24.09	-12.15	27.54	-37.93	-88.51	-43.69	-2.63	29.34	43.79	-14.57	-11.94

Table 4. Comparison of twenty-five pairs of the same surface measurements. Each measurement in each pair is the average of $K = 1, 2\ldots, 25$ scannings (Sample S_1).

K	RMSE(K)	AD(K)	RAD(K)	CORR(K)
1	29.9206	24.3918	39.34	0.976197
2	16.1997	12.2270	19.72	0.991638
3	12.0631	9.1397	14.74	0.995344
4	9.5787	7.2473	11.69	0.997058
5	8.0759	6.0922	9.83	0.997907
6	7.2181	5.4557	8.80	0.998326
7	6.4875	4.9875	8.04	0.998647
8	5.9424	4.4872	7.24	0.998864
9	5.4966	4.1483	6.69	0.999028
10	5.2196	3.8716	6.24	0.999156
11	4.9286	3.7250	6.01	0.999260
12	4.8247	3.5197	5.68	0.999340
13	4.7255	3.5833	5.78	0.999422
14	4.4789	3.4893	5.63	0.999498
15	4.4706	3.4192	5.51	0.999562
16	4.3470	3.3203	5.36	0.999604
17	4.2757	3.2708	5.28	0.999649
18	4.1745	3.1889	5.14	0.999682
19	4.1218	3.1536	5.09	0.999715
20	4.0364	3.0038	4.84	0.999749
21	3.9972	2.9587	4.77	0.999783
22	3.9334	2.9078	4.69	0.999806
23	3.8863	2.8604	4.61	0.999828
24	3.8373	2.8461	4.59	0.999851
25	3.7989	2.8046	4.52	0.999872

Table 5. Comparison of twenty-five pairs of the same surface measurements. Each measurement in each pair is the average of $K = 1, 2\ldots, 25$ scannings (Sample S_2).

K	RMSE(K)	AD(K)	RAD(K)	CORR(K)
1	29.4196	24.2045	39.65	0.976385
2	15.8359	12.1613	19.83	0.991685
3	11.7407	9.1049	14.80	0.995363
4	9.2811	7.2314	11.72	0.997066
5	7.7933	6.0879	9.84	0.997909
6	6.9441	5.4578	8.80	0.998326
7	6.2208	4.9942	8.03	0.998645
8	5.6812	4.4989	7.23	0.998862
9	5.2398	4.1634	6.67	0.999025
10	4.9656	3.8895	6.22	0.999153
11	4.6775	3.7444	5.98	0.999256
12	4.5746	3.5411	5.65	0.999337
13	4.4764	3.6041	5.75	0.999419
14	4.2323	3.5110	5.60	0.999495
15	4.2241	3.4416	5.48	0.999560
16	4.1017	3.3437	5.33	0.999602
17	4.0311	3.2947	5.25	0.999647
18	3.9309	3.2136	5.11	0.999680
19	3.8788	3.1787	5.05	0.999713
20	3.7942	3.0304	4.80	0.999747
21	3.7554	2.9857	4.73	0.999781
22	3.6923	2.9353	4.65	0.999804
23	3.6456	2.8884	4.57	0.999827
24	3.5971	2.8743	4.55	0.999850
25	3.5591	2.8332	4.48	0.999871

MEASUREMENT SCIENCE REVIEW, **17**, (2017), No. 6, 282-289

DE GRUYTER OPEN

MEASUREMENT SCIENCE REVIEW

Journal homepage: http://www.degruyter.com/view/j/msr

ISSN 1335-8871

Alternative Methods for Estimating Plane Parameters Based on a Point Cloud

Roman Stryczek

University of Bielsko-Biala, Faculty of Mechanical Engineering and Computer Science, Department of Production Engineering and Automation., Willowa 2, Bielsko-Biała, Poland, rstryczek@ath.bielsko.pl

Non-contact measurement techniques carried out using triangulation optical sensors are increasingly popular in measurements with the use of industrial robots directly on production lines. The result of such measurements is often a cloud of measurement points that is characterized by considerable measuring noise, presence of a number of points that differ from the reference model, and excessive errors that must be eliminated from the analysis. To obtain vector information points contained in the cloud that describe reference models, the data obtained during a measurement should be subjected to appropriate processing operations. The present paperwork presents an analysis of suitability of methods known as RANdom Sample Consensus (RANSAC), Monte Carlo Method (MCM), and Particle Swarm Optimization (PSO) for the extraction of the reference model. The effectiveness of the tested methods is illustrated by examples of measurement of the height of an object and the angle of a plane, which were made on the basis of experiments carried out at workshop conditions.

Keywords: Robotic inspection, plane detection, Particle Swarm Optimization, RANSAC, Monte Carlo Method.

1. INTRODUCTION

There has been continuous development of flexible means of production in recent years, and it included industrial robots and fast and accurate laser displacement sensors that allow for non-contact measurement techniques. This encourages engineers to design fully automated quality control operations carried out directly at a production workshop. Benefits that can be achieved here include full automation of measurements that are often carried out in an environment that is hostile to man, improvement of objectivity of measurements by eliminating the human error, holding of information about the quality of produced machine parts in the early stage of the manufacturing process, and fuller use of the potential of industrial robots installed on production lines. The fact that a measurement made using a laser beam is a non-contact measurement makes it possible to avoid a collision between the measuring sensor and an object, measurement of hard-to-reach surfaces, often dirty or hot. Results of measurements of geometrical dimensions achieved with this method are not as reliable as in the case of measurements made in measurement laboratories. To reduce these differences simulation methods to assess measurement strategies and determine components of uncertainty of measurements carried out in accordance with a chosen strategy need to be developed.

The measurement result is always different from the unknowable actual value of a measured quantity. This is mainly due to the imperfection of measuring instruments and measurement techniques and the conditions of making measurements. Therefore, the result of a measurement without providing its accuracy is not that meaningful. The measure of accuracy of a measurement is the uncertainty of measurement that characterizes the dispersion of values that can be reasonably attributed to the measurand.

The actual value of the measurand is unknowable, so the measurement error is unknowable as well. Measurement errors can be grouped into three categories: random errors, systematic errors, and excessive errors. A complete measuring procedure should provide the possibility of classification of error into one of these categories. When identifying an excessive error, the measurement must be rejected and repeated. In case of systematic errors their value must be assessed and/or a method of compensation must be developed. Random errors are errors caused by an accidental effect of a large number of intangible interfering factors the total impact of which changes with the next measurement. Thus, measurement uncertainty should primarily concern the characteristics of random errors. The uncertainty of measurement based on which a product is qualified as one that complies with requirements must be in a proper relation to the tolerance of a controlled quantity. The uncertainty budget of measurement normally contains several components of measurement uncertainty. Determining which components of uncertainty are important in the context of tolerance of measurement is one of the main tasks of a technician that compiles measurement results.

DOI: 10.1515/msr-2017-0035

The use of techniques of statistical analysis is becoming a standard in the field of measurement uncertainty estimation [1], [2], [3]. The Monte Carlo simulation method (MCM) was developed in the 1940's by S. Ulamowski. MCM is used for mathematical modelling of processes that are far too complex to be able to predict their results using an analytical approach. Sampling according to the selected distribution of values characterizing the process plays an important role in MCM. After collecting a sufficiently large amount of such information its characteristics can be compared with the observed experimental results, confirming or denying the validity of assumptions made in the entire procedure. The accuracy of a result obtained by this method depends on the number of checks and the quality of the random number generator.

Currently, there are more effective methods to browse through decision-making space, often multi-dimensional, than MCM, which are also random in nature. These include a group of methods based on a paradigm of a cluster of particles moving in n-dimensional space. The direction and rate of movement of individual particles is partly determined by their inertia, the best location remembered, and the location of the best located particles in the entire cluster. Applying these simple rules in simulation models, it is possible to speed up the search for a satisfactory solution and/or improve their quality.

The efficiency of determining the estimated model parameters using random methods depends mainly on the number of dimensions of decision-making space and on the possibility to limit the search scope in a given dimension. As shown in paper [4], the possibility of using discrete decision-making space accelerates the time to generate results and improve its quality.

The presented paper concerns a study on measurement possibilities carried out by means of an LK-H152 triangulation sensor with an LK-G5001P controller mounted on a flange of a 6-axis industrial robot with anthropomorphic kinematics (Fig.1.). Results of coordinate measurements, which we deal with in the course of measurement by laser sensor, are subject to errors of designation of position and orientation of the reference system and errors of designation of position and orientation of measured surface relative to the reference system. To make a correct determination of a measuring instrument coordinate system (TCP), a laser beam detector dedicated to this task was developed.

This article presents results of research on measurements carried out in a direction that is parallel to the laser beam, bypassing the problem of detecting the edge of an object in directions that are perpendicular to the laser beam. A measurement made in a direction that is parallel to the beam can identify planes, for example. Therefore, measurements of height, parallelism of planes, angle between planes and plane surface flatness deviations are possible. Such measurements, like any other measurement, are subject to a degree of uncertainty. In this paper the focus is on an important component of uncertainty which is the uncertainty of the calculation method used to determine the plane model. Another important component of uncertainty in this type of measurements is the laser sensor reading error that is related to the relaxation time of the measurement system. This error for this position was analyzed [5]. Therefore, the adopted period of relaxation in the conducted experiments was constant at 1 second. Errors resulting from the robot's failure to achieve the programmed position were compensated for by a direct reading of the actual final position of the robot arm to which the measuring sensor was attached. Such a behavior is acceptable in cases where we are sure that the axes of the robot are accurately calibrated. Due to small values, the reading error of the actual position by the robot's measuring systems was considered measurement noise compensated by the increased number of measurement points.

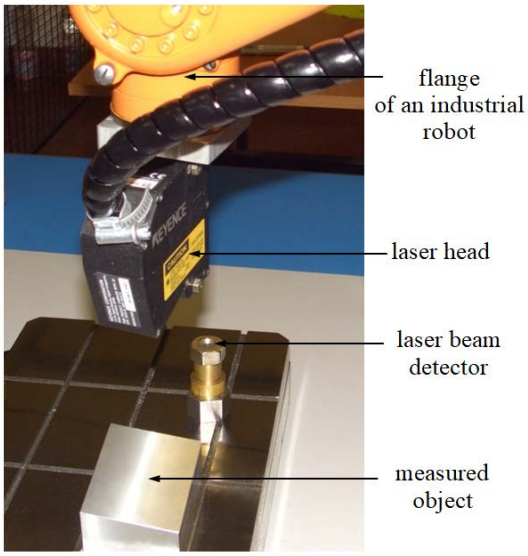

Fig.1. General view of the test bench.

Determination of a correct model for the measurement of geometrical values may give rise to various difficulties. Estimation of uncertainty of coordinate measurements is a very complex task due to the diversity of measured characteristics, strategies, and measurement methods. Therefore, the analytical estimation of uncertainty of coordinate measurements should be supported by specialist software [6].

2. ROUGH DETERMINATION OF PLANE USING RANSAC

RANSAC algorithm [7], [8] is an iterative method used to estimate sought parameters of the mathematical model of object based on a redundant set of data points, forming a cloud around the determined area. This collection, in addition to the points located very close to the area, also contains many points burdened with measurement noise; there may also appear excessive errors. The algorithm essentially comprises two repeated iterative phases: initialization and test. Initialization phase consists of random selection of a minimum set of points needed for an unequivocal determination of the estimated parameters of model geometry and to determine the parameters of this model. The identified model is a hypothesis, which is tested in the next phase - test. During the test, the distance of remaining points of data from

the created model is calculated. In the original formulation of the algorithm by Fischler and Bolles [7], criterion for assessing the quality of the model is the size of a set of consensus *card(CS*). *CS* consists of points, the distance of which from the model is less than the threshold δ. The selection of an appropriate δ value is essential for the stability of the RANSAC algorithm and has an essential impact on the quality of separated surfaces, in addition to the number of iterations. Fig.2. illustrates how the size of CS changes depending on δ threshold and selected arbitrary number of *iter* iterations of the RANSAC algorithm. It can be observed that for small *iter* the graph is monotonic, and the obtained *card(CS)* values are understated, especially for small δ, which proves the possibility of missing the best solutions. The problem of the number of iterations is critical in cases of application of the RANSAC method for the extraction of planes on the basis of point cloud with a significant number, order of several hundred thousand and more. Execution time for calculations can be in these cases fatal. In this work's experiments the sum of points does not exceed 1000, so the calculation time was negligible compared to the time of measurement.

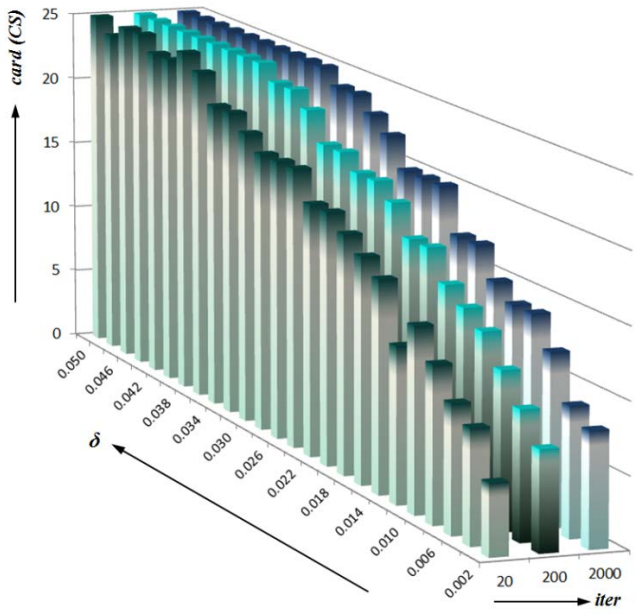

Fig.2. Evolution of *card(CS)* depending on δ and the number of *iter* iterations of the RANSAC algorithm.

According to [9], the value of δ can be determined on the assumption that all measuring points are subject to errors with normal distribution. Central limit theorem states that with more random variables influencing the performance of measurement, the distribution is close to normal. We are dealing with such a situation during measurements with laser sensor installed on the robot flange, carried out under the conditions of the production workshop.

For a given normal distribution with a known standard deviation σ the δ parameter allows to determine the probability of given point *p* belonging to the *CS* according to the dependence:

$$p = \frac{1}{2}\left(1 - erf\left(\frac{\delta}{\sigma\sqrt{2}}\right)\right) \tag{1}$$

where:

erf – error function,

σ – standard deviation.

Modifications proposed in [9] reduce the processing time, allowing dynamic selection of an appropriate number of iterations, successively amended after each appointment of better model. The number of additional *iter* iterations is determined according to (2) and is:

$$iter = \frac{\log(1-P)}{log\left(1-\frac{(card(CS))^3}{N(N-1)(N-2)}\right)} \tag{2}$$

where:

P – probability of identifying the correct plane,

card(CS) – the size of *CS* set,

N – number of all measuring points of data set.

Fig.3. illustrates how *iter* parameter changes for small *N*=const=25 and δ=const=0.03. Fig.4. illustrates how to form the output variables of *card(CS)*, *NCS* - the number of iterations required to achieve a given *CS*, *Add* - the number of additional iterations, during which the result and *Total* were not improved - the total number of iterations. These results were obtained for *P*=0.999 and *N*=25.

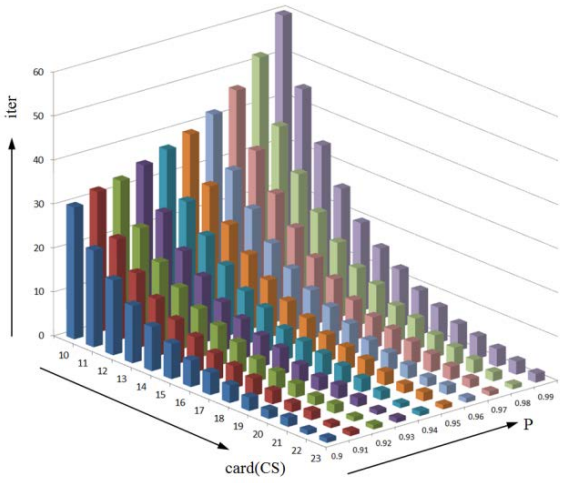

Fig.3. The evolution of number of iterations according to the size of the current set of CS consensus and the probability *P* of identification of the best model for the number of measurement points *N*=25 i δ=0.03 mm.

As is apparent from Fig.4., the necessary number of iterations does not exceed 250 in any trial as compared to the number of permutations of three-element sample with 25-element set of 13800 and it is the result justifying the use of the proposed approach. RANSAC method, as proposed by its creators, does not guarantee that the resulting solution is optimal for the threshold δ. Therefore, there are works in which the authors propose to consider additional criteria, improving the quality of solution. In reference [10], the following rule to change the model was proposed:

$$\left.\begin{array}{c} card(CS) > \max\limits_{card}(CS)\ or \\ card(CS) = \max\limits_{card}(CS)\ and\ \sigma < \min\_\sigma \end{array}\right\} \quad (3)$$

where:
$\max_{card}(CS)$ – maximum reached cardinality of *CS*,
min_σ – minimum value of the standard deviation for the models for which $card(CS) = \max_{card}(CS)$.

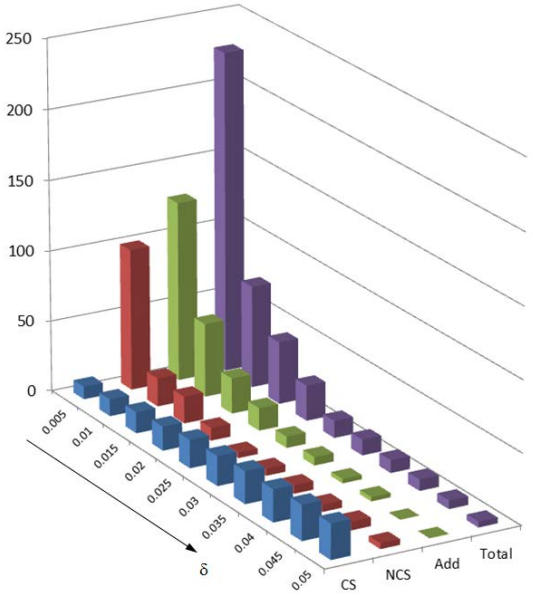

Fig.4. Development of cardinality of *CS* set and the number of iterations required to achieve these results depending on pre-set threshold δ.

RANSAC method, although effective in the case of very large sets of points cannot be included in the precise methods for the measurement of small area and with a small number of measuring points. The method assumes that the three points are randomly selected to a designated plane, while each point is defined with unknowable error. Therefore, the determined plane can only be regarded as an approximation of the optimal solution. Nevertheless, the RANSAC method can significantly reduce the search area, and thus accelerate the effect of more accurate methods.

3. Estimation of Position and Orientation of the Plane by Random Methods

The search for solution through random search of decision space of estimated model parameter is a recognized and even a preferred method of finding solutions [1], [3]. To reduce the likelihood of omission of the optimal solution, to improve the quality of solutions and at the same time to reduce the computation time it is very beneficial to limit the size of search area of conditions. In case of estimating position and orientation of plane, the RANSAC method can be used.

Let the estimated plane associated with the coordinate system XYZ_E in reference coordinate system XYZ_R (Fig.5.) determine displacement vector of coordinate origin $\overrightarrow{RE}=[x_R, y_R, z_R]^T$ and differential vector of orientation $\overrightarrow{RE}=[x_R, y_R, z_R]^T$. Vector $\overrightarrow{R"E'}$ can be clearly determined by giving its r and the angle of rotation γ around Z'_R axis. This allows to determine the components of the X and Y axis. The third component in the Z-axis results from the assumption that the vector has unit length. Decisive area in the above premise will be five-dimensional, and its parameters are x_R, y_R, z_R, r, γ. Origin of the unit normal vector of the estimated plane is inside a sphere with a center at point R and radius ρ, while its end is on the area of sphere segment embedded at point E, with unit radius and angle 2ε. Parameters ρ and ε define in this case the size of decisive area in search for the best suited plane. Number of degrees of freedom of determined model can easily be limited to three, after the adoption of easy to accept assumptions: determined plane is not parallel to Z_R axis, point E lies on Z_R axis and component Z of vector $\overrightarrow{RE}$ has a direction agreeing with the Z_R axis. Then the decisive area has only three dimensions z_R, r, γ, which significantly speeds up the process of estimating the correct plane. The position of decisive area in the latter case changes dynamically, as component Z_r is set to a range $\pm dZ$ with respect to the best currently achieved solution.

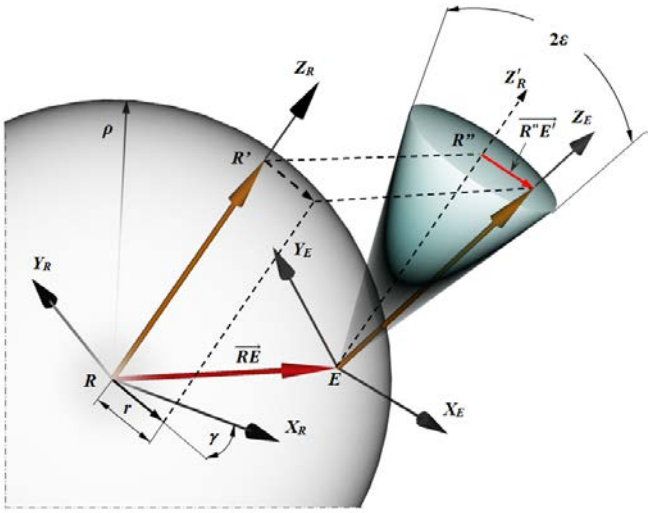

Fig.5. Reciprocal linking of geometric size in estimation position and orientation of the plane.

MCM method applied to solve the task of estimating the best suited plane is based on random generation of model of the plane, and then verification of the model fitting to the measuring point cloud. Each point in the above defined five-dimensional decisive area represents one plane. Repeating the cycle of generation and test several times, we were able to reach a satisfactory solution. Match criterion of generated plane to the point cloud is usually the minimum sum of squared distances of measurement points of the estimated plane. MCM is therefore simple to implement, even directly in the control system of an industrial robot. The only requirement is access to the proper quality of random number generator.

A more advanced, but also random method of searching the state space is first proposed by the Kennedy and Eberhart method of swarm of particles [11]. Basis of optimization methods derives from the natural behavior of living individuals, living and moving in large clusters as fish, birds, bees, etc. Each individual (particle) is determined to achieve the best position in the swarm, guaranteeing it survival, access to food and/or reproduction. Hence, the movement vector of particle (Fig.6.) to a new position $\overrightarrow{P_aP_n}$ is the result of three components: inertia component of particle $\overrightarrow{P_aP_1}$ determined as part of the motion vector in the previous iteration cycle, a component resulting from the best position of particle in the swarm $\overrightarrow{P_1P_2}$, and the component resulting from the best position so far memorized by the particle $\overrightarrow{P_2P_n}$.

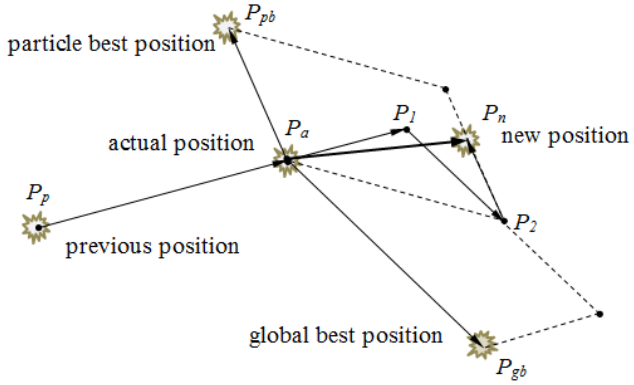

Fig.6. Determination of the new position of particle in the method of PSO.

Movement of the particle in subsequent movements described by the equation:

$$\left.\begin{aligned}\overrightarrow{P_aP_n} &= \overrightarrow{P_aP_1} + \overrightarrow{P_1P_2} + \overrightarrow{P_2P_n}\\ \overrightarrow{P_aP_1} &= w_1R_1\overrightarrow{P_pP_a}\\ \overrightarrow{P_1P_2} &= w_2R_2\overrightarrow{P_aP_{gb}}\\ \overrightarrow{P_2P_n} &= w_3R_3\overrightarrow{P_aP_{pb}}\end{aligned}\right\} \quad (4)$$

where:

w_1, w_2, w_3: weight of individual components,

R_1, R_2, R_3: random numbers in the range [0,1] of the normal distribution.

Many researchers are trying to introduce the modifications to the basic PSO algorithm [4], [12], [13]. They focus mainly on the dynamic control of weights of individual components. Positive results can be achieved by setting initial low weight w_2, which ensures uniform penetration throughout the decisive area through swarm, in the first phase of the algorithm. In turn, determination of high level of w_2 in the final phase causes the particles to penetrate the closed area exactly at the best solution, which allows further improvement of the solution. It is also proposed to introduce a global factor of speed of the particle, allowing reducing the value of position correction in the final phase of the algorithm. Authors' own experience shows that properly chosen and dynamically adjusted speed of particles has a decisive influence on the efficiency of PSO algorithm. Another line of modifications concerns the resignation of globally best representative of the population in favor of locally best representatives within a certain environment. Further modifications can affect the introduction of braking mechanism of the particles in the event of leaving the acceptable area. Alternatively, the solution is killing the particle after crossing the allowable area and generating in its place a new particle. This latter approach brings the PSO algorithm closer to the genetic algorithm.

PSO method in the context of the search for the best suited plane requires in its first chase of swarm initialization generating a set of unit vectors, embedded inside a sphere with center at the reference radius ρ (Fig.7.a)), or embedded in a section of Z_r axis (Fig.7.b)). During this phase the best-defined particle of pre-generated random collection is found. Drawn position of the particle is initially recognized as the best position of the particle. This phase does not differ from the MCM method. In the next iteration steps, each particle changes its position according to (3). The algorithm on-line modifies the best position of the particle and particle with globally best position in the whole swarm.

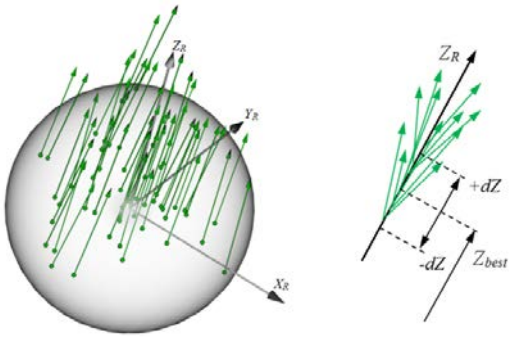

a) generated inside the sphere. b) generated on a section of Z axis.

Fig.7. Swarm of unit vectors.

4. Result of Conducted Tests

The object of the study were two basic objects in the form of master plate (Fig.8.a)) and a rectangular body in which the upper area was beveled with respect to the base at an angle of about 10° (Fig.8.b)). For the master plate height research was conducted, whereas the second object was set in four different positions (0°, 90°, 180°, and 270°), in each case in order to determine the angle between the base area and the top area.

The first stage of tests compared the speed of the method and sensitivity of the results achieved on the size of decisive area, characterized by parameters dZ and ε. The test results allow to conclude that MCM (Fig.9.) requires a very large number of iterations to achieve satisfactory results. In the present test, the criterion was to achieve a standard deviation of less than 0.019. MCM is also very sensitive to increase in the decisive area. Doubling the dimensions of decisive area increased the computation time 10 times. In case of the PSO method (Fig.10.), the number of iterations to achieve a satisfactory outcome fluctuated at the level of less than 5000, without showing visible dependence on dimensions of the decisive area. Given the size of the population of particle swarm (50), the calculation time for obtaining criterion was 4 times less than in the case of MCM.

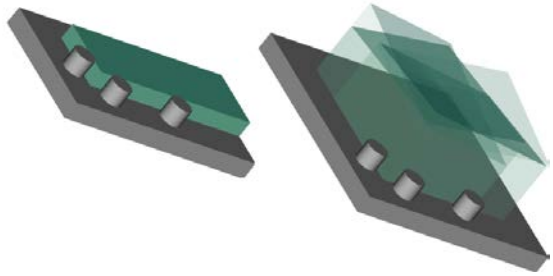

a) Master plate. b) Cuboid with a beveled wall.

Fig.8. Measured object.

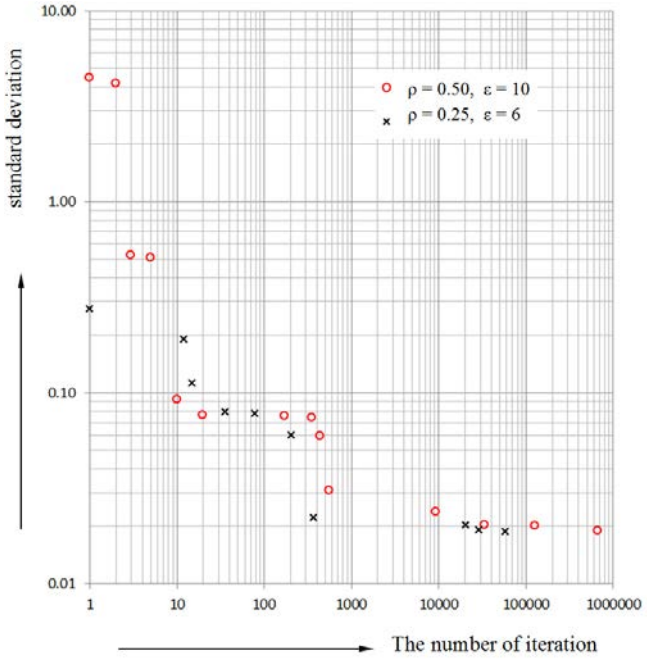

Fig.9. Examples of two courses of the RANSAC+MCM algorithm.

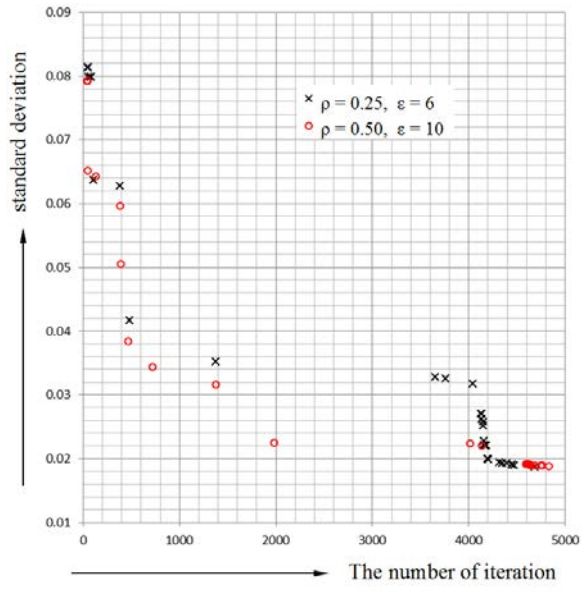

Fig.10. Examples of two courses of the RANSAC+PSO algorithm.

For the determination of uncertainty components arising solely from the computational method a series of tests on the same measurement data was carried out, each repeated 25 times. The results of computation of plane position in the Z axis and the angle of the plane in relation to the reference plane were shown in Table 1. Differences in the reproducibility of each method are best illustrated in Fig.11. and Fig.12., representing graphs of probability density, assuming that the distributions are normal.

Table 1. Test results illustrating reproducibility of calculation methods.

	Z position, mm		Angle, …°	
Method	average	Std. Dev.	average	Std. Dev.
RANSAC	9.853	0.0071	10.289	0.0131
PSO	9.843	0.0036	10.293	0.0070
RANSAC+MCM	9.836	0.0047	10.268	0.0072
RANSAC+PSO	9.849	0.0018	10.286	0.0028

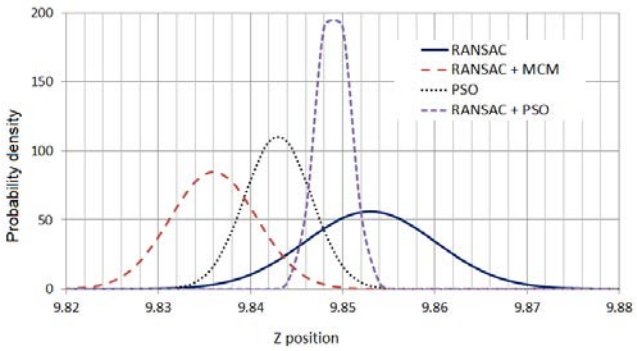

Fig.11. Comparison of repeatability of four methods of calculation when determining the position of the plane in Z axis.

Table 2. shows calculation results of the angle of inclination of the top plane of measured object (Fig.8.b)) to the base plane in four different angular settings relative to the base. The calculation was carried out in four methods described above.

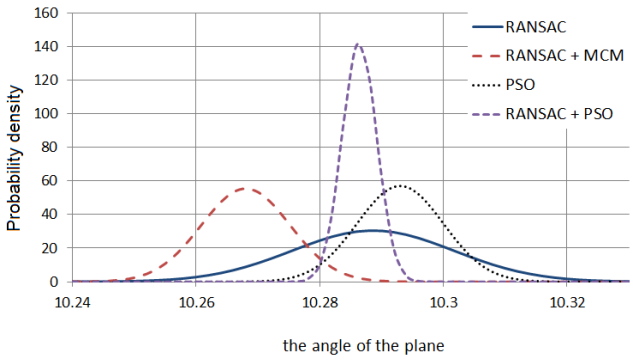

Fig.12. Comparison of repeatability of four methods of calculation when determining the angle of the plane in relation to the reference plane.

Table 2. Results of measurements of the angle of inclination of inclined area.

Method	position	number of tests	min ...°	max ...°	average ...°	std. dev. ...°
RANSAC	0°	25	9.994	10.115	10.039	0.034
	90°	25	10.168	10.255	10.217	0.023
	180°	25	10.234	10.315	10.286	0.025
	270°	25	10.179	10.266	10.218	0.023
	All	100	9.994	10.315	10.190	0.096
RANSAC + MCM	0°	25	9.991	10.126	10.039	0.040
	90°	25	10.212	10.265	10.239	0.016
	180°	25	10.214	10.336	10.286	0.037
	270°	25	10.201	10.256	10.225	0.015
	All	100	9.991	10.336	10.197	0.099
PSO	0°	25	9.968	10.032	9.994	0.017
	90°	25	10.141	10.283	10.223	0.045
	180°	25	10.280	10.321	10.303	0.010
	270°	25	10.160	10.240	10.197	0.020
	All	100	9.968	10.321	10.179	0.095
RANSAC + PSO	0°	25	9.991	10.031	10.007	0.010
	90°	25	10.308	10.333	10.320	0.007
	180°	25	10.263	10.289	10.280	0.007
	270°	25	10.128	10.158	10.139	0.009
	All	100	9.991	10.333	10.187	0.124

The best is the RANSAC + PSO method. The standard deviation score for each of the four different settings does not exceed in this case 0.01°. At the same time this RANSAC + PSO method is best illustrated by the fact (Fig.12.) that in the case of measuring the same surface in various settings of the object one should expect a certain discrepancy of results. In order to obtain the results of the measurements of normal vector components of the plane subject to a low rate of uncertainty, you should take in the same position of the object and previously eliminate systematic error by taking into account the results of pattern measurement of the angle, carried out in the same position and in the same workshop conditions.

Table 3. shows the results of measurement of height of the plate, by designating the position of base plane and the upper plane. Measurements of the height of the plate with micrometer device showed differences in the height of the plate in the area 8.998÷9.005. Presented results relate to the corners of the plate with the greatest height. Results of conducted tests of measurement of height of the object with laser sensor also prefer the RANSAC + PSO method, for which the standard deviation is less than half than for the RANSAC method alone.

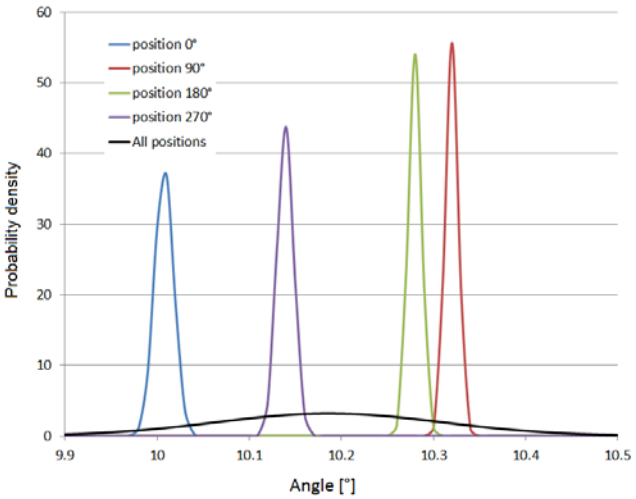

Fig.13. Dispersion of the results of the measurement of angle of inclination of plane using RANSAC+PSO.

Table 3. Results of measurements of the height of master plate.

Method	number of tests	Min [mm]	Max [mm]	Average [mm]	std. dev.
RANSAC	25	8.981	9.037	9.012	0.013
RANSAC+MCM	25	8.982	9.029	9.006	0.011
PSO	25	8.996	9.027	9.013	0.008
RANSAC+PSO	25	9.000	9.018	9.014	0.006

5. SUMMARY

The presented paper shows four approaches to estimation of the position and orientation of the plane based on a cloud of scanned points. The RANSAC method, although simple to implement, can only roughly estimate the parameters of the studied plane. However, it allows the removal of excessive errors that may appear in a cloud of scanned measurement points. It also radically reduces the search area, in the next phase of accurate estimation of parameters of the plane. The Monte Carlo method is also easy to implement, but it needs a very large number of iterations to achieve a satisfactory result. The rationale for its use is when we are able to reduce the search area to a very small size and calculation time is not too important. The PSO method is very effective, but has a developed algorithm that also needs to be adjusted by carrying out a series of simulation tests. This requires more experience and competence from the person using this algorithm. A combination of RANSAC with random optimization methods gives the best results both in terms of time to generate results and their quality.

All considered methods in a wide range use random values and statistical functions. Unfortunately, control systems of industrial robots and controllers of optical triangulation sensors do not offer this type of feature as standard. In order to use these methods more widely in practical solutions, manufacturers of industrial robot controllers should equip them with software richer in this regard.

On the basis of the experience it can be said that the current state of the art measuring equipment used and the methodology of calculations, maintaining the proper diligence measurement workshop, can be used for measurements of length tolerated within a range ± 0.05 mm. In case of angular dimensions, the result of the measurement is strongly dependent on the size of the measured area.

It would be a natural continuation of the above research to solve the problem of determining the plane using a mobile robot. Due to the extent of the issue, this may be the subject of another scientific paper.

REFERENCES

[1] Ferrero, A., Salicone, S. (2004). A Monte Carlo-like approach to uncertainty estimation in electric power quality measurement. *COMPEL*, 23 (1), 119-132.

[2] Jing, H., Huang, M.F., Zhong, Y.R., Kuang, B., Jiang, X.Q. (2007). Estimation of the measurement uncertainty based on Quasi Monte-Carlo Method in optical measurement. In *International Symposium on Photoelectronic Detection and Imaging 2007: Optoelectronic System Design, Manufacturing, and Testing*. SPIE 6624, 10 p.

[3] Joint Committee for Guides in Metrology. (2008). *Evaluation of measurement data - Supplement 1 to the "Guide to the expression of uncertainty in measurement" - Propagation of distributions using a Monte Carlo method*. JCGM 101:2008.

[4] Stryczek, R., Pytlak, B. (2014). Multi-objective optimization with adjusted PSO method on example of cutting process of hardened 18CrMo4 steel. *Eksploatacja i Niezawodnosc – Maintenance and Reliability*, 16 (2), 236-245.

[5] Stryczek, R., Dutka, P. (2016). The analysis of signal disruptions from the optical triangulation measurement sensor. *Measurement Automation Monitoring*, 62 (2), 62-65.

[6] Płowucha, W., Jakubiec, W. (2015). Coordinate measurement uncertainty: Models and standards. *Technisches Messen*, 82 (1), 1-6.

[7] Fischler, M.A., Bolles, R.C. (1981). Random sample consensus: A paradigm for model fitting with applications to image analysis and automated cartography. *Communications of the ACM*, 24 (6), 381-395.

[8] Zuliani, M. (2014). *RANSAC for Dummies*. Technical Report, http://old.vision.ece.ucsb.edu/~zuliani/docs/RANSAC4Dummies.pdf.

[9] Hartley, R., Zisserman, A. (2004). *Multiple View Geometry in Computer Vision, Second Edition*. Cambridge University Press.

[10] Yang, M.Y., Förstner, W. (2010). *Plane detection in point cloud data*. Technical Report Nr. 1/2010, University of Bonn, Germany.

[11] Kennedy, J., Eberhart, R. (1995). Particle swarm optimization. In *IEEE International Conference on Neural Networks*.

[12] Chen, W.N., Zhang, J., Chung, H.S.H., Zhong, W.L., Wu, W.G., Shi, Y.H. (2010). A novel set-based particle swarm optimization method for discrete optimization problems. *IEEE Transactions on Evolutionary Computation*, 14 (2), 278-300.

[13] Poli, R., Kennedy, J., Blackwell, T. (2007). Particle swarm optimization, *Swarm Intelligence*, 1 (1), 33-57.

Received August 26, 2017.
Accepted November 13, 2017.